

A primary cell-based *in vitro* model of the human small intestine reveals host olfactomedin 4 induction in response to *Salmonella* Typhimurium infection

Thomas Däullary ^{a,b}, Fabian Imdahl ^c, Oliver Dietrich ^c, Laura Hepp^a, Tobias Krammer ^c, Christina Fey ^d, Winfried Neuhaus ^{e,f}, Marco Metzger ^{a,d,g}, Jörg Vogel ^{c,h}, Alexander J. Westermann ^{c,h}, Antoine-Emmanuel Saliba ^c, and Daniela Zdzieblo ^{a,d,g}

^aChair of Tissue Engineering and Regenerative Medicine, University Hospital Würzburg (UKW), Würzburg, Germany; ^bFaculty of Biology, Biocenter, Chair of Microbiology, Julius-Maximilians-Universität Würzburg (JMU), Würzburg, Germany; ^cHelmholtz-Institute for RNA-based Infection Research (HIRI), Helmholtz Centre for Infection Research (HZI), Würzburg, Germany; ^dFraunhofer Institute for Silicate Research (ISC), Translational Center Regenerative Therapies (TLC-RT), Würzburg, Germany; ^eAustrian Institute of Technology (AIT), Vienna, Austria; ^fDepartment of Medicine, Faculty of Medicine and Dentistry, Danube Private University (DPU), Krems, Austria; ^gFraunhofer Institute for Silicate Research, Project Center for Stem Cell Process Engineering, Würzburg, Germany; ^hInstitute for Molecular Infection Biology (IMIB), University of Würzburg, Würzburg, Germany

ABSTRACT

Infection research largely relies on classical cell culture or mouse models. Despite having delivered invaluable insights into host-pathogen interactions, both have limitations in translating mechanistic principles to human pathologies. Alternatives can be derived from modern Tissue Engineering approaches, allowing the reconstruction of functional tissue models *in vitro*. Here, we combined a biological extracellular matrix with primary tissue-derived enteroids to establish an *in vitro* model of the human small intestinal epithelium exhibiting *in vivo*-like characteristics. Using the foodborne pathogen *Salmonella enterica* serovar Typhimurium, we demonstrated the applicability of our model to enteric infection research in the human context. Infection assays coupled to spatio-temporal readouts recapitulated the established key steps of epithelial infection by this pathogen in our model. Besides, we detected the upregulation of olfactomedin 4 in infected cells, a hitherto unrecognized aspect of the host response to *Salmonella* infection. Together, this primary human small intestinal tissue model fills the gap between simplistic cell culture and animal models of infection, and shall prove valuable in uncovering human-specific features of host-pathogen interplay.

ARTICLE HISTORY

Received 13 November 2022
Revised 3 February 2023
Accepted 22 February 2023


KEYWORDS


Intestinal enteroids; biological scaffold; *Salmonella* Typhimurium; OLFM4; NOTCH; filamentous *Salmonella* Typhimurium; bacterial migration; bacterial virulence; 3D tissue model; olfactomedin 4; infection

Introduction

The gastrointestinal mucosa forms a barrier that shields the human body from a variety of contaminants and pathogenic agents. However, enteric pathogens have evolved specific mechanisms to overcome this barrier¹. A detailed understanding of the underlying virulence mechanisms is therefore important for the development of effective therapeutic treatments of infectious diseases. Importantly, the structural, biological, and physico-chemical properties of the gastrointestinal mucosa affect the infection process and the associated host responses. Therefore, the models used in infection research need to adequately recapitulate these aspects – ideally, in a human context.

In the last decade, pluripotent stem cell (PSC)-derived organoids or adult stem cell (ASC)-derived enteroids gained popularity for modeling the human intestinal epithelium *in vitro*^{2–7}. Cultured in specified media and embedded in Matrigel® — a biological extracellular matrix (ECM) — they exhibit certain characteristics of the native tissue, yet show an inverted architecture with the apical cell surface facing the lumen of the organoid. Alternatively, epithelial stem cells can be seeded and grown as two-dimensional (2D) monolayers on top of synthetic scaffolds^{8,9}. This enables apical and basolateral accessibility, but requires coating with an ECM-like substance such as Matrigel®, collagen, or gelatin, for cellular attachment and growth. Both enteroid/

CONTACT Daniela Zdzieblo  daniela.zdzieblo@uni-wuerzburg.de  Institute for Silicate Research - Project Center for StemCell Process Engineering and Translational Center Regenerative Therapies, University Hospital Würzburg - Chair of Tissue Engineering and Regenerative Medicine, Röntgenring 11, Würzburg 97070

 Supplemental data for this article can be accessed online at <https://doi.org/10.1080/19490976.2023.2186109>

© 2023 The Author(s). Published with license by Taylor & Francis Group, LLC.

This is an Open Access article distributed under the terms of the Creative Commons Attribution-NonCommercial License (<http://creativecommons.org/licenses/by-nc/4.0/>), which permits unrestricted non-commercial use, distribution, and reproduction in any medium, provided the original work is properly cited. The terms on which this article has been published allow the posting of the Accepted Manuscript in a repository by the author(s) or with their consent.

organoid or 2D monolayer-based models of the small intestinal epithelium have contributed significantly to our understanding of fundamental principles of gut biology in general and tissue-specific immunity in particular^{8–10}. Likewise, when used as host models of infection, they improved our understanding of the pathogenesis of diverse viral and bacterial pathogens^{9,11–15}.

We have previously combined a biological, organ-specific ECM scaffold (small intestinal submucosa; SIS) with human primary tissue-derived enteroids in a Transwell®-like system¹⁶. The resulting *in vitro* model of the human small intestinal epithelium displays an *in vivo*-like compartmentalization with high physiological performance, recapitulating the apical-basolateral polarity of the native tissue¹⁶. However, the complex setup of the previously published model in a closed bioreactor with dynamic flow conditions restricts the versatile application in infectious disease research, since throughput and standardization are limited in addition to technical challenges.

In the present work, we therefore adapted the model setup to a static and open system with adjusted cultivation conditions, which facilitates handling and increases the throughput of the *in vitro* models. The optimized human small intestinal epithelium model (hITM) is characterized by a monolayer with appropriate barrier functions and resembles *in vivo*-like cellular phenotypes as demonstrated by immunohistochemistry and single-cell RNA-seq. Using *Salmonella enterica* serovar Typhimurium (STm) as a representative enteric pathogen, we demonstrated the suitability of the hITM as an *in vitro* infection model. Specifically, the hITM model was effectively infected by STm, and recapitulated key steps of the infection process. Besides, we revealed the enhanced expression of olfactomedin 4 (OLFM4) in STm-infected cells, a previously unrecognized aspect of the host cell response to this pathogen. Together, this work introduces a primary cell-based *in vitro* system of the human small intestinal epithelium and illustrates its use as a host model for enteric infection research.

Results

The hITM resembles morphological, morphometric, and structural key features of the human small intestinal epithelium

We introduced a revised version of our previously published Transwell®-like model of the hITM, combining a porcine-derived ECM scaffold (SIS) with intestinal epithelial cells (IECs) isolated from human enteroid cultures (Figure 1a). Major novelties in the set-up of the hITM are as follows: 1) the extended time frames for the controlled proliferation of IECs on the ECM scaffold, 2) the used culture medium during proliferation as well as 3) the prolonged differentiation time to derive functional cellular subtypes of the intestinal epithelium under static cell culture conditions. In addition, we also extended our analysis panel to comprehensively characterize the hITM regarding morphological, morphometric, functional, molecular, and cellular features. Human intestinal tissue biopsies or enteroid cultures grown in Matrigel® were used as references as indicated below.

To get first insights into the tissue structure of the hITM, histological analyses were performed. Native intestinal tissue samples served as controls. Alcian blue staining revealed typical compartmentalization of the native small intestinal epithelium characterized by alternating villus and crypt domains with a highly polarized columnar monolayer in the villus region and the existence of mucin positive cells (Figure 1 a1, a2). Similar, to the native tissue, a confluent and polarized IEC monolayer formed in the hITM (Figure 1a3) with a mucin layer covering its apical region (Figure 1 a4, a5). In comparison to the native tissue, mucin inclusion bodies and mucin positive cells appeared to be differently distributed in the hITM.

As cellular polarity is key for the functionality of the intestinal epithelium, we next evaluated this feature within the hITM by quantitatively determining the cell height based on F-actin cytoskeleton staining and observed a mean cell height of 32.76 μm ($\pm 5.99 \mu\text{m}$) which is within the range of the cell height reported for the native tissue (30–43 μm , according to PT and MN, 1993¹⁷ (Figure 1 b)). Furthermore, the polarized IEC monolayer developed a tight barrier with a mean transepithelial

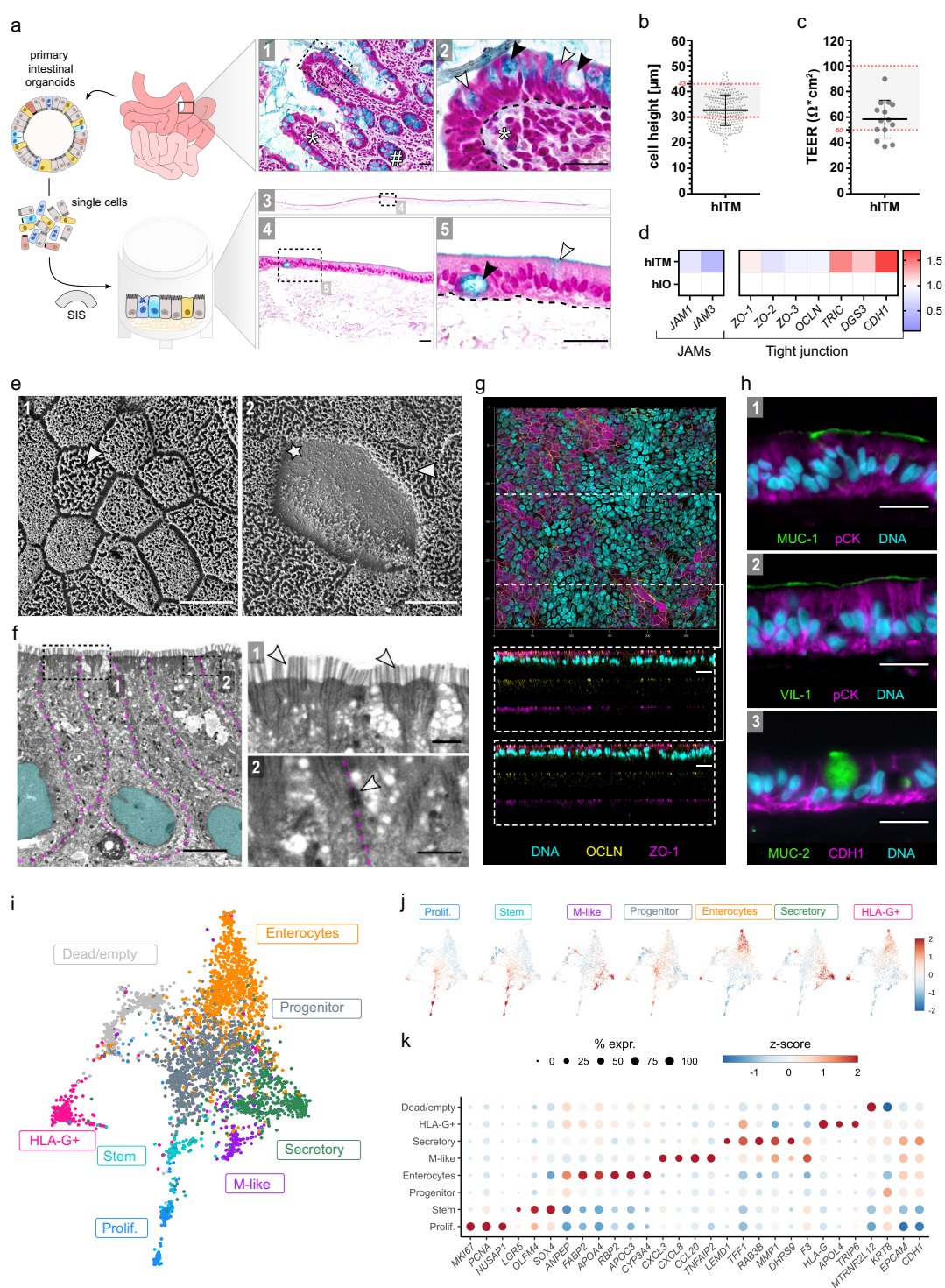


Figure 1. IECs develop a monolayer on a biological scaffold with *in vivo*-like tissue characteristics in a Transwell®-like setup. **Aa left** Experimental workflow: IECs were isolated from small intestinal biopsies followed by expansion as enteroids in 3D Matrigel®-embedded culture as previously reported⁷. for hITM establishment, dissociated enteroids were seeded as single cells on a biological SIS scaffold in a Transwell®-like setup. **a right** Representative histochemical Alcian blue staining of the native human small intestinal mucosa (**top**, $n = 3$) in comparison to the epithelial monolayer in the hITM (**bottom**, $n = 3$). Glycosylated proteins, typically mucins, are stained in blue, whereas nuclei are stained in deep purple and cell cytoplasm in light purple. Scale bar: 25 μm . **a1** Cross-section of the native human small mucosa with compartmentalization into villus (*) and crypt (#) domains. Scale bar: 25 μm . **a2** Magnification of the villus region shown in a1 highlighting the columnar structure of the cells organized as epithelial monolayer. The white arrowheads depict individual cells filled with mucins. The black arrowheads point toward mucin inclusion bodies and the dashed line indicates separation of the epithelial layer from the underlying connective tissue. Scale bar: 25 μm . **a3** Cross-section of the hITM showing the epithelial cell layer in deep purple and the underlying SIS scaffold in light purple. Scale bar: 25 μm . **a4** Magnification

electrical resistance (TEER) value of $58.46 \Omega \cdot \text{cm}^2$ ($\pm 18.83 \Omega \cdot \text{cm}^2$) that is similar to the TEER value published for native tissue samples ($50\text{--}100 \Omega \cdot \text{cm}^2$, according to Srinivasan et al., 2015¹⁸ (Figure 1 c)). In line with the TEER measurements, gene expression analysis of junction associated molecules (JAMs; *JAM 1*: 0.79-fold; *JAM 2*: 0.42-fold) and further tight junction (TJ) associated genes (Zonula Occludens, *ZO-1*: 1.06-fold; *ZO-2*: 0.76-fold, *ZO-3*: 0.89-fold; Occludin, *OCLN*: 0.90-fold) demonstrated comparable expression levels in cells isolated from the hITM and human enteroid samples that have been used as reference in the high-throughput qRT-PCR analysis. Of note, expression values obtained for Tricellulin (*TRIC*), Desmoglein-3 (*DSG3*) and Cadherin-1 (*CDH1*) were increased in hITM-derived cells (*TRIC*: 1.44-fold, *DSG3*: 1.21-fold *CDH1*: 1.68-fold) compared to enteroids of human origin.

Next, we performed electron microscopy (EM) to gain insights into the ultrastructural organization of the hITM (Figures 1 e, 1 e) and observed a polygonal cobblestone-like arrangement of the IEC monolayer (Figure 1 e1) and its decoration

with typical microvilli structures (Figure 1 f1). Some cells lacked microvilli characterizing them as Microfold (*M-*) cells (Figure 1 e2)¹⁹. In addition, ultrastructural analyses highlighted desmosomes as well as TJ formations between cells in the apical region (Figure 1 f2), that were verified via immunohistochemical (IHC) stainings against ZO-1 and OCLN (Figure 1 g). Additionally, IHC analyses revealed a “honeycomb”-like pattern between individual cells and a concentrated localization of ZO-1 and OCLN signals at the apical cell borders (Figure 1 g).

In the final step of hITM characterization, we evaluated whether the adapted differentiation in the novel protocol leads to an *in vivo*-like cellular diversity in the hITM model. Thus, we first investigated the expression and localization of typical intestinal proteins via IHC (Figure 1 h) and could demonstrate positive signals for Mucin-1 (*MUC-1*; Figure 1 h1), a transmembrane mucin expressed in the gut epithelium on the apical side of individual cells and cell clusters²⁰, Villin-1 (*VIL-1*; Figure 1 h2), a brush border protein localized to the microvilli, broadly but exclusively expressed on the apical cell surface^{21,22},

of the hITM demonstrating IECs lining the apical surface of the SIS as a confluent monolayer. Scale bar: 25 μm . **a5** Magnification of A4 highlighting the apical-basolateral polarity of the epithelial monolayer in the hITM, the presence of a mucin layer on top of the IECs as well as representative mucin+ cells (white arrowhead marks a cell filled with mucins; black arrowhead points at a cell with a mucin inclusion body). Scale bar: 25 μm . **b** Mean cellular height calculated from the measurements of 256 individual IECs within the hITM ($n = 4$, 64 cells per biological replicate); dotted red lines mark the physiological range of 30–43 μm , according to PT and MN, 1993¹⁷. **c** Mean TEER value measured in the hITM ($n = 3$, each with >4 independent technical replicates); dotted red lines indicate the physiological range of 50–100 $\Omega \cdot \text{cm}^2$ reported for the native human intestinal epithelium according to Srinivasan et al., 2015¹⁸. **d** Heat map showing the gene expression profile for *JAM1* and 3 as well as tight junction associated proteins (*ZO -1,-2,-3*, *OCLN*, *TRIC*, *DSG3*, *CDH1*). Expression in the hITM was compared to the expression in human enteroids. Data were obtained by high-throughput qPCR and were normalized to the expression level observed for enteroid samples ($n = 1$). **e** Representative SEM images of the hITM apical surface revealing IECs decorated with microvilli (**e1**; white arrow head) as well as M-like cells characterized by typical folds and the absence of microvilli (**e2**; white star) ($n = 2$). Scale: 1 μm . **f** Representative TEM pictures of a hITM cross section. Cell borders are indicated by dashed lines in magenta, while nuclei are presented in cyan ($n = 2$). Scale bar: 5 μm . **f1** Magnification of the apical cell region with closely arranged, upright microvilli (white arrowhead). Scale bar: 1 μm . **f2** Magnification of the cell-cell border in the apical region with indicated desmosome formation (white arrowheads). Scale bar: 1 μm . **g** Top view of representative IHC images of the hITM stained for *OCLN* (yellow) and *ZO-1* (magenta) with side view of the cellular monolayer at the indicated regions (dashed line) ($n = 3$). DAPI counterstaining is shown in blue. Scale bar: 20 μm . **h** Representative IHC stainings of the hITM demonstrating the expression of characteristic intestinal proteins including *MUC-1* (green), *VIL-1* (green), *MUC-2* (green), pCK (magenta) and *CDH1* (magenta). Cell nuclei are visualized by DAPI counterstaining shown in blue ($n = 3$). Scale bar: 20 μm . **i** UMAP projection of 3,952 single-cell transcriptomes from two models color coded according to assigned cell types. **j** Cell embedding (as in **i**) showing scaled, log-normalized gene expression of cell type markers (see supplement table 1). **k** Dot plot showing the cluster average of scaled, log-normalized gene expression of cell type markers. IECs: intestinal epithelial cells, hITM: human small intestinal epithelial tissue model, SIS: small intestinal submucosa, TEER: transepithelial electrical resistance, JAM: junction associated molecule, ZO: Zona Occludens, OCLN: Occludin, TRIC: Tricellulin, DSG3: Desmoglein-3, CDH1: Cadherin-1, SEM: scanning electron microscopy, TEM: transmission electron microscopy, TJ: tight junction, IHC: immunohistochemistry, *MUC-1*: Mucin-1, *VIL-1*: Villin-1, *MUC-2*: Mucin-2, pCK: pan-Cytokeratin, M-like cells: microfold-like cells.

and Mucin-2 (MUC-2; [Figure 1 h3](#)), a mucin secreted by goblet cells, albeit rarely observed as an intracellular signal in only a few hITM cells.

The hITM epithelium consists of a heterogeneous cell composition, resembling major cell types of the native tissue

In order to extend the cell-type classification within the *in vitro* model, we applied droplet-based single-cell RNA-seq. In total 3,360 cells were analyzed with 21,645 identified genes (4,814 median genes per cell, 23,123 median counts per cell). Unsupervised clustering of cells in the hITM ([Figure 1 i](#)) revealed eight populations with distinct transcriptional phenotypes. Based on cell type-specific gene expression signatures, five populations could be annotated to respective IEC subtypes ([Figure 1 j-k](#)). Transit amplifying (TA) cells were defined as “proliferation cluster” based on genes involved in cell cycle regulation (*MKI67*: Marker Of Proliferation Ki-67, *PCNA*: Proliferating Cell Nuclear Antigen, *NUSAP1*: Nucleolar And Spindle Associated Protein 1)^{23–26} and represented 6.7% of the total cell number. The “stem cluster” comprises stem cells identified by the expression of typical intestinal stem cell markers (*LGR5*: Leucine Rich Repeat Containing G-Protein Coupled Receptor 5, *OLFM4*: Olfactomedin-4, *SOX4*: SRY-Box Transcription Factor 4)^{23–26}, accounting for 3.5% of all cells. The “progenitor cluster” constitutes 29.8% of all cells classified based on the relative absence or downregulation of marker genes specific for differentiated epithelial subtypes. Enterocytes (*enterocytes cluster*) accounted for 28.9% of all cells. Immature enterocytes were defined by their expression of *ANPEP* (*Alanyl Aminopeptidase, Membrane*), *FABP2* (*Fatty Acid Binding Protein 2*) and *APOA4* (*Apolipoprotein 4*), while mature enterocytes were characterized based on their expression of *RBP2* (*Retinol Binding Protein 2*), *APOC3* (*Apolipoprotein C3*) and *CYP3A4* (*Cytochrome P450 Family3 Subfamily A Member 4*)^{23–26}. Around 4% of all cells belonged to the “M-like cluster” expressing the corresponding cell type-specific genes (*CXCL3*: C-X-C Motif Chemokine Ligand 3, *CCL20* C-C-Motif Chemokine Ligand 20, *TNFAIP2*: TNF Alpha-Induced Protein 2)^{23,25,27,28} as well as immune-associated genes such as *CXCL8* (*C-X-C Motif Chemokine Ligand 8*). A sixth cluster was defined as secretory-like cells (*secretory cluster*),

accounting for 16.4% of all cells expressing *LEMD1* (*LEM Domain Containing 1*), *TFF1* (*Trefoil Factor 1*)^{24,29}, *RAB3B* (*Member RAS Oncogene Family*)^{30,31}, *MMP1* (*Matrix Metalloproteinase 1*), *DHRS9* (*Dehydrogenase/Reductase 9*)³² and *F3* (*Coagulation Factor III*). In addition, the combined expression of general epithelial cell markers along with *HLA-G* (*Major Histocompatibility Complex, Class I, G*), *APOL4* (*Apolipoprotein 4*), and *TRIP6* (*Thyroid Hormone Receptor Interactor 6*) defined a seventh population classified as “*HLA-G+ cell cluster*” (10.6%). The high expression of the mitochondrial gene *MTRNR2L12* (*MT-RNR2 Like 12*, pseudogene) in combination with a low number of genes/counts determined a low quality cell cluster representing dead/fragmented cells. All clusters were positive for the expression of the general epithelial markers *KRT8* (*Keratin 8*), *EPCAM* (*Epithelial Cell Adhesion Molecule*), and *CDH1*.

STm infection of the hITM recapitulates main stages of human infection

Having demonstrated that the hITM recapitulates key characteristics of the human intestinal epithelium, we next studied infection of this model by an exemplary enteropathogenic bacterium ([Figure 2a](#)). For that, we used a GFP-expressing STm strain that allowed us to track the bacteria within the tissue model during the infection process. The infection protocol (see material and methods for details) involved the administration of STm to the apical compartment of the hITM, an incubation for 1 h at 37°C during which the bacteria invaded the host cells, followed by a high-dose gentamicin treatment to inactivate the remaining extracellular bacteria. Thereafter, a low dose of gentamicin was constantly applied to prevent reinfection by cell-released bacteria ([Figure 2a](#)).

Via microscopic analysis, we observed STm attached to the apical brush border surface of the hITM at the 1 h time point ([Figure 2 b](#)). Membrane perturbations in the vicinity of extracellular STm ([Figure 2 b](#)) might indicate STm-induced membrane ruffling and ongoing STm invasion. In order to evaluate the membrane ruffling in more detail, we stained our infected hITM for the cytoskeletal protein F-actin and focused on structural

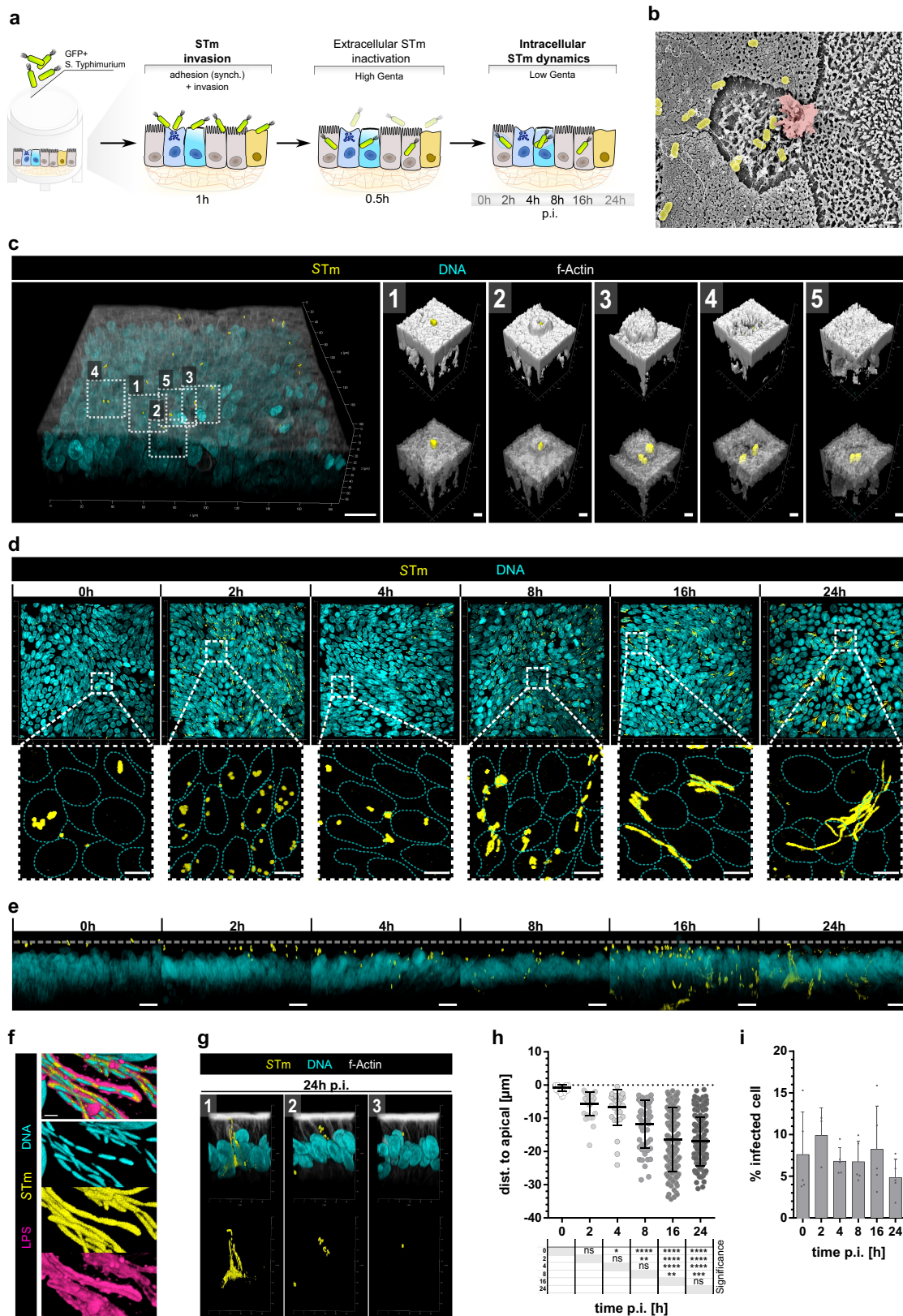


Figure 2. Invasion characteristics of *Salmonella* Typhimurium in the hITM. **Aa** Schematic depiction of the STm infection process. hITMs were inoculated with STm expressing GFP by administration to the apical compartment. Incubation at 37°C allowed bacterial adhesion and invasion of epithelial cells. After 1 h, extracellular bacteria were killed by high-gentamicin treatment of the hITM (50 µg/ml) for 0.5 h, followed by a medium-exchange to low-gentamicin conditions (10 µg/ml) for the rest of the assay. Samples were taken and analyzed at 0 h, 2 h, 4 h, 6 h, 8 h, 16 h and 24 h p.i. **b** Representative SEM images of infected hITM 1 h p.i. highlighting invasion by

alterations in proximity of GFP-expressing STm (Figure 2 c). In doing so, we recapitulated the characteristic steps of STm invasion³³: (1) adherence, (2) initiation of F-actin remodeling and (3) F-actin ruffling, (4) reestablishment of the F-actin layer and bacterial entry, and (5) restoration the F-actin cytoskeleton (Figure 2 c 1–5).

We further evaluated spatial localization of the bacteria via confocal microscopy and 3D projection with subsequent spatial image analysis (Figure 2 d, e). Our data show that the bacteria were exclusively intracellular and that the hITM integrity was maintained after infection, as indicated by the comparable distribution of cellular nuclei (Figure 2 d, top row). Interestingly, morphologies and relative intracellular localizations of bacteria changed over time (Figure 2 d). Immediately after infection (0 h p.i.), mainly individual STm bacteria and only a few cluster-forming colonies were detected in infected IECs. With ongoing cultivation, increased frequencies of those clusters were observed, especially at 8 h post infection. Of note, a few structures that appeared more elongated with diffuse edges were visible at 8 h p.i. and became dominant from 16 h p.i. onwards. These structures likely reflect bacteria blocked in the cellular division process and hence adopting a filamentous morphology (Figure 2 f). Additionally, we observed infected cells, which carried singular or multiple non-filamentous bacteria at each individual time point,

thereby indicating heterogeneity in intracellular STm populations.

Within their host cells, STm were detected apically of the nuclei, in close proximity to the apical membrane of the epithelium at 0 h p.i. (Figure 2 e, g). From 4 h p.i. onwards, STm were predominantly observed at the same horizontal positioning as the cellular nucleus and from 8 h p.i. on, also on the basolateral side of the epithelium. Simultaneously with the emergence of filamentous STm at 16 h p.i., STm-specific GFP signals were detected at higher frequencies at the basal site of infected cells, indicating the migration of certain bacteria within the IEC monolayer. Interestingly at 24 h p.i., the elongated STm structures stretched over the complete cell, from the apical to the basal side (Figure 2 e, g1), while STm without an elongated shape seemed to be randomly distributed along the apical-basolateral axis (Figure 2 g2, g3). We determined the localization of individual bacteria in relation to the apical cell membrane and revealed significant changes over time. The mean distance of STm from the apical to the basolateral side was $-0.82 \mu\text{m}$ ($\pm 0.99 \mu\text{m}$) at 0 h p.i., $-5.64 \mu\text{m}$ ($\pm 3.44 \mu\text{m}$) at 2 h p.i., $-6.74 \mu\text{m}$ ($\pm 5.34 \mu\text{m}$) at 4 h p.i., $-11.70 \mu\text{m}$ ($\pm 7.23 \mu\text{m}$) at 8 h p.i., $-16.34 \mu\text{m}$ ($\pm 9.70 \mu\text{m}$) at 16 h p.i. and $-16.97 \mu\text{m}$ ($\pm 7.27 \mu\text{m}$) at 24 h p.i. (Figure 2 h). Together, this indicates a time-dependent migration of STm toward the basolateral side of infected cells. In addition, flow

protuberances of the infected IEC membrane (red) and STm (yellow) on top of the IEC brush border in close proximity to the microvilli ($n = 2$). Scale bar: $1 \mu\text{m}$. **c** Apical membrane area of the STm-infected hITM 1 h p.i. Representative 3D surface rendered images taken by confocal microscopy revealed sequential invasion steps characteristic for STm ($n = 5$). GFP expressing STm are depicted in yellow and F-actin stained by Phalloidin in gray. DAPI counterstaining is shown in cyan. Scale bar: $20 \mu\text{m}$ and scale bar in c1–5: $1 \mu\text{m}$. **d** Representative microscope images (top view on 3D projection) of STm-infected hITMs 0 h–24 h p.i. highlighting the existence of filamentous STm observed at 16 h and 24 h p.i. GFP expressing STm are shown in yellow and nuclear counterstaining by DAPI in cyan. Top panel represents merged images and the bottom panel visualizes STm-specific GFP signals in yellow as well as dotted cyan lines indicating nuclei. Scale bar: $5 \mu\text{m}$ ($n = 3$). **e** Side view on 3D projections from **d** showing intracellular migration of STm within the hITM over time. Dotted line indicates apical actin layer. Scale bar: $10 \mu\text{m}$ ($n = 3$). **f** Representative image of intracellular filamentous STm depicting bacterial DNA (cyan), bacterial cytoplasm with GFP (yellow), and the continuous bacterial membrane with LPS (magenta). Scale bar: $1 \mu\text{m}$ ($n = 3$). **g** Representative images from **e** of heterogeneous STm stages in individual host cells at 24 h p.i.: (1) formation of filamentous STm, (2) STm forming clusters, and (3) STm as single bacteria. Scale bar: $10 \mu\text{m}$ ($n = 3$). **h** Graph showing the quantification of the mean bacterial intracellular migration distance, given as negative distance from the apical membrane surface, of individual STm (analyzed number of bacteria per time point: 0 h: 43, 2 h: 34, 4 h: 32, 8 h: 52, 16 h: 204, 24 h: 185). Significance values are shown in the table below the graph. Significance was calculated by ordinary one-way ANOVA and Tukey's multiple comparisons test with ****= $p \leq 0.0001$, ***= $p \leq 0.001$, **= $p \leq 0.01$, *= $p \leq 0.05$, ns= $p > 0.05$. Insignificant p-values are not displayed. **i** Bar diagram depicting the mean percentage with standard deviation of infected epithelial cells at 0 h, 2 h, 4 h, 8 h, 16 h, 24 h p.i. Infection rate was determined by measuring the relative proportion of GFP+ cells in the whole host cell population by flow cytometry ($n = 3–5$). STm: *Salmonella* Typhimurium, p.i.: post infection, SEM: scanning electron microscopy, IEC: intestinal epithelial cell, hITM: human intestinal tissue model.

cytometric detection of the GFP signal emitted by STm revealed a stable infection rate of 7.35% ($\pm 1.54\%$) within the hITM over the time course of 24 h (Figure 2 i).

STm infection in the hITM results in the elevated expression of *OLFM4* in infected IECs

Next, we analyzed the response of our hITM model to STm infection. We profiled the expression of markers characteristic for intestinal cell types via qRT-PCR. Our data show that the mRNA levels of *VIL1*, a representative marker of mature enterocytes, and *LYZ*, a marker expressed by Paneth cells, were unchanged during the course of infection. Likewise, the expression of the canonical stem cell marker *LGR5* was not significantly altered upon STm infection. In contrast, we observed increased expression values for *MUC1*, a transmembrane mucin expressed in the gut epithelium, and *OLFM4*, another common ISC marker (Figure 3 a).

In light of the emerging role of *OLFM4* in the context of infectious diseases (Liu and Rodgers, 2022), we sought to validate the STm-induced upregulation of *OLFM4* mRNA via an independent method. By HCR-FISH analysis, we compared *OLFM4* mRNA levels in STm-infected and uninfected hITMs. As shown in Figure 3 b, only few *OLFM4*⁺ cells were detected in the infected hITM as well as the mock control immediately after infection (0 h p.i.), presumably representing ISCs, which — according to our scRNA-seq data (Figure 1 i-k) — represent a minority in the model with a frequency of 3.5%. While the expression level of *OLFM4* remained unchanged over 24 h in the mock control, we observed an increased *OLFM4* expression in the infected hITM from 4 h p.i. onwards (Figures 3 b, c). Quantification by HCR-FlowFISH (Figure 3 c) revealed a significantly increased percentage of *OLFM4*⁺ cells in the STm-infected cell population from 4 h to 24 h p.i. ($2.28\% \pm 1.45\%$ at 0 h p.i.; $8.81\% \pm 5.18\%$ at 4 h p.i.; $11.76\% \pm 4.60\%$ at 8 h p.i.; $18.50\% \pm 5.08\%$ at 16 h p.i.; $31.50\% \pm 8.01\%$ at 24 h p.i.). In comparison, the percentages of *OLFM4*⁺ bystander cells were significantly lower ($2.08\% \pm 1.32\%$ at 0 h p.i.; $1.86\% \pm 0.71\%$ at 4 h p.i.; $2.46\% \pm 0.78\%$ at 8 h p.i.; $2.26\% \pm 1.57\%$ at 16 h p.i.; 3.42%

$\pm 0.53\%$ at 24 h p.i.). Similarly, lower frequencies were observed for *OLFM4*⁺ cells in the uninfected mock control ($1.32\% \pm 0.30\%$ at 0 h p.i.; $0.34\% \pm 0.13\%$ at 4 h p.i.; $0.42\% \pm 0.02\%$ at 8 h p.i.; $2.81\% \pm 2.32\%$ at 16 h p.i.; $3.44\% \pm 1.00\%$ at 24 h p.i.). Interestingly, our HCR-FISH analysis demonstrated that the *OLFM4* levels correlate with bacterial numbers (GFP signal intensity per infected host cell), as shown by the representative microscope image depicted in Figure 3 d. In this context, we further measured an elevated median fluorescence intensity (MFI) of GFP, expressed by STm, at 16 h p.i. and 24 h p.i. in the *OLFM4*⁺ cells (Figure 3 e), indicating a link between the bacterial load of individual STm-infected cells and the upregulation of *OLFM4*. Along with the MFI of GFP, the MFI for *OLFM4* showed an increasing trend in *OLFM4*⁺ cells over time (Figure 3 f). Together, these data suggest a link between the bacterial load of individual STm-infected cells and the upregulation of *OLFM4* in the hITM.

STm-mediated *OLFM4* induction depends on NOTCH signaling

In the healthy gut, intestinal *OLFM4* expression is predominantly restricted to the stem cell population residing in the crypt compartment, and regulated by the NOTCH pathway³⁵. To confirm a role for the NOTCH pathway in the elevated expression of *OLFM4* in STm-infected hITM, we measured *OLFM4* expression in the infected hITM treated with DAPT, a γ -secretase inhibitor of the NOTCH pathway (Figure 4 a). For quantification, we normalized the HCR-FISH intensity against the number of nuclei (Figure 4 b).

Immediately after infection, we detected similar *OLFM4* signals in the infected hITM (MOI 10), the infected hITM treated with DAPT (MOI 10 + DAPT) and the uninfected control (mock) (Figure 4 a). In line with the data shown in Figure 3, we observed a significant increase of *OLFM4* levels in the infected model as early as 4 h p.i., with further upregulation at 16 h and 24 h after infection (Figure 4 b). From 16 h p.i. onwards, the *OLFM4* expression not only significantly increased in infected samples but also dropped when the infected hITM was treated with DAPT. Similar effects were seen at 24 h p.i. with a significantly

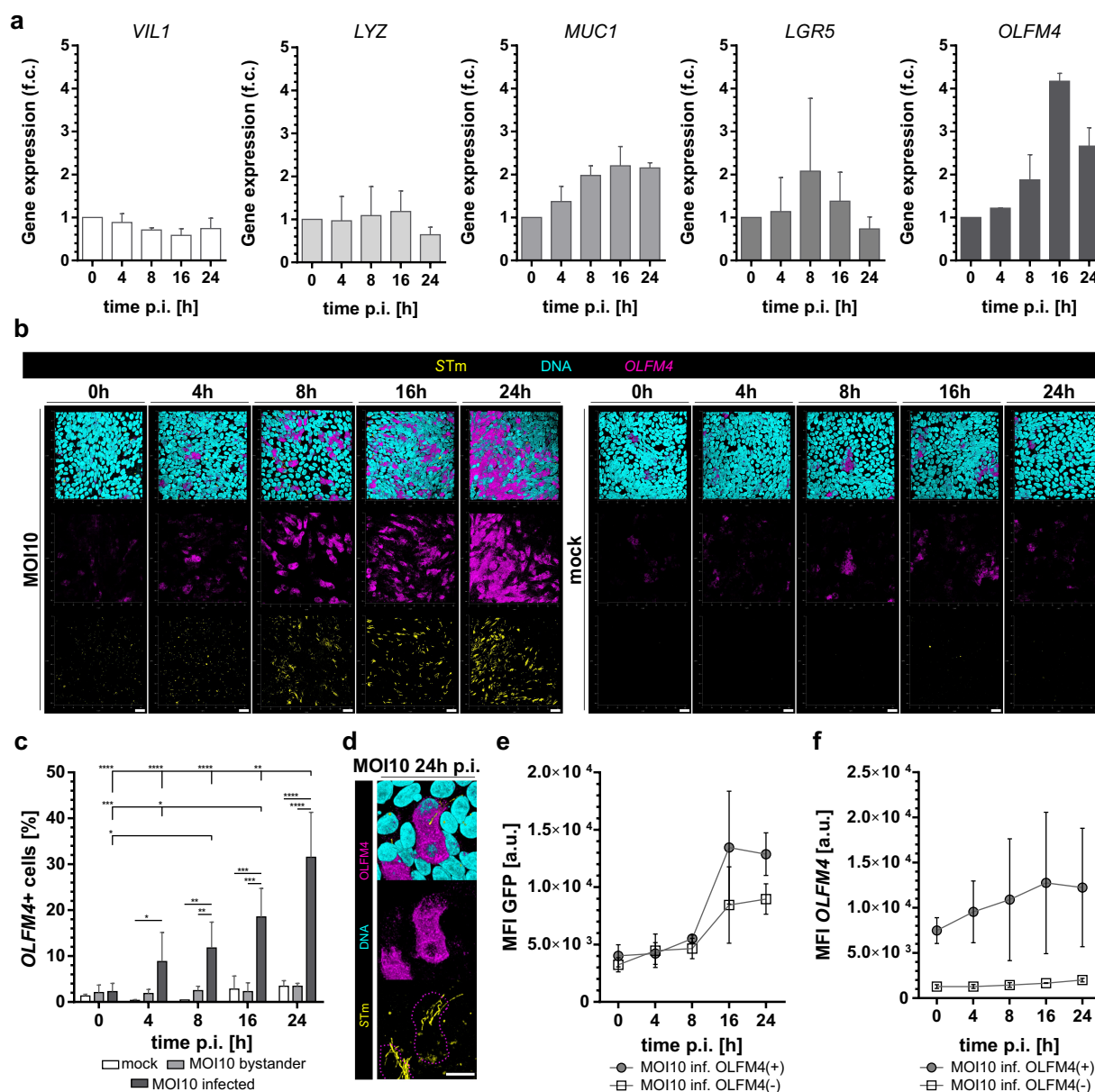


Figure 3. *OLFM4* is upregulated in *STm*-infected cells. **Aa** qRT-PCR-derived gene expression of *VIL1*, *LYZ*, *MUC1*, *LGR5*, and *OLFM4* in *STm*-infected tissue models from 0 to 24 h p.i. Expression is depicted as a fold change relative to 0 h p.i. ($n = 2$) and was calculated using the $\Delta\Delta CT$ method³⁴. Human *Ef1a* was used as a reference mRNA. **b** Top view on 3D projections of representative fluorescent images of *STm*-infected hITM (MOI10, left) and uninfected hITM controls (mock, right). *OLFM4* expression (magenta) becomes visible at 4 h p.i. with ongoing increase of expression over time. GFP expressing *STm* are shown in yellow and DNA counterstaining in cyan ($n = 2$). **c** Frequency of *OLFM4*+ IECs in infected hITM (MOI10 infected) at the indicated time points compared to uninfected mock controls as well as in the population of non-infected bystander cells (MOI10 bystander), detected via HCR-Flowfish ($n = 3$; minimum 10,000 cells). Significance was calculated via matching two-way ANOVA with statistically significant differences and Tukey's multiple comparisons test. **d** Representative microscope pictures of *STm*-infected hITM (MOI10) at 24 h p.i., demonstrating the restriction of increased *OLFM4* expression to infected cells ($n = 3$). **e** MFI of GFP in infected *OLFM4*+ and *OLFM4*- IECs ($n = 3$). **f** MFI of *OLFM4* in infected *OLFM4*+ and *OLFM4*- IECs at 0 h-24 h p.i. measured via HCR-Flowfish ($n = 3$). Significance is indicated with ****= $p \leq 0.0001$, ***= $p \leq 0.01$, **= $p \leq 0.01$, *= $p \leq 0.05$. Insignificant p-values are not displayed. *OLFM4*: Olfactomedin 4, *STm*: *Salmonella* Typhimurium, p.i.: post infection, hITM: human intestinal tissue model, IEC: intestinal epithelial cell, MFI: median fluorescence intensity, HCR-FlowFISH: Hybridization Chain Reaction Fluorescent in-Situ Hybridization coupled with flow cytometry.

increased *OLFM4* expression in the infected hITM compared to DAPT-treated or uninfected models.

Of note, the *OLFM4* signal intensities in infected and DAPT-treated models matched those of

uninfected controls. Importantly, the observed patterns of *OLFM4* mRNA levels were reflected at the protein level, as revealed by immunofluorescence (Figure 4 d). The intracellular growth of STm – as inferred from the mean fluorescence intensity per infected IEC – was unaffected by the DAPT treatment (Figure 4 c). Interestingly, under infection conditions, the filamentous STm form was observed in cells with high *OLFM4* protein levels (Figures 3 b and 4 e). DAPT treatment of the infected hITM prevented STm filamentation (Figure 4 d). Quantification of this observation revealed significantly decreased filament lengths in DAPT-treated hITM (MOI 10 + DAPT; median: 3.00, 25%/75% percentile: 2.40/4.05) compared to untreated hITM (MOI 10; median: 3.50, 25%/75% percentile: 2.54/5.49) at 24 h p.i. (Figure 4 e). Together, our data support that DAPT-mediated NOTCH inhibition interferes with *OLFM4* expression in the hITM epithelium and seems to counteract STm filamentation.

Discussion

Given the key role of the intestinal epithelium as the main barrier of the body to the environment³⁶, it is important to replicate physico-chemical, structural, and biological properties of this tissue *in vitro*. Here, we refined a previously published method from our group to engineer a Transwell®-like model of the human small intestinal epithelium grown under static cell culture conditions by combining a porcine-derived, organ-specific ECM and primary tissue-derived enteroids (referred to as hITM)^{16,37}. Epithelial key features of the hITM were consistent with previous reports³⁸ and comparable to the native tissue^{17,18}. The intestinal epithelial phenotype was validated by the expression of key markers including the transmembrane-expressed MUC1 and VIL1, expressed on the apical surface of intestinal epithelial cells^{21,22}. Structural similarity of the hITM to the native intestinal epithelium is further highlighted by a distinct polygonal, cobblestone arrangement of individual cells that are covered by microvilli^{36,39}. Tissue-specific epithelial junction complexes (JC) including TJ, adherens junctions (AJ), and desmosomes were formed between individual cells of the epithelial monolayer. Not only did we detect a tissue-

specific JC expression profile, but also the distinct spatial arrangement of JC proteins in the model. For example, similar to the native tissue, the TJ-associated proteins ZO-1 and OCLN were observed in the apical region of the cells, whereas desmosomes were localized in the lower cell regions as well as laterally³⁶. Interestingly, compared to Matrigel®-based enteroid cultures, hITM cells showed increased gene expression values for specific TJ proteins such as *TRIC*, a structurally specialized TJ protein as well as for *CDH1*, a major constituent of AJ, and for *DSG3*, a desmosomal cadherin. The increased expression of *TRIC*, *DSG3*, and *CDH1* could be related to the planar arrangement and the pronounced polarization of the cells grown on the biological ECM scaffold.

In addition to the structural features, we further demonstrated that the hITM is composed of cellular phenotypes similar to those observed in the native epithelium. RNA-seq analysis at the single-cell level showed that the hITM is composed of stem cells, highly proliferative TA progenitor cells, and differentiated cell types, such as enterocytes and cell types with a transcriptional profile similar to secretory cells. The cell types were classified according to specific gene expression patterns. An M-like cell cluster was defined by *CCL20*, *TNFAIP2*, *CXCL8*, and *CXCL3* expression^{23–26,40}, supporting the findings observed by EM analysis. According to Nakamura et al., 2018, mature M-cells express *SPIB* (Spi-B transcription factor) and *GP2* (Glycoprotein 2)⁴¹. However, none of these genes were detected in our scRNA-seq analysis, implying an immature M-cell phenotype in our hITM. In the native tissue, M-cell development is tightly regulated via RANKL signaling, a factor secreted by stromal cells^{25,42,43}. The lack of stromal cells and the consequent absence or diminished RANKL signaling possibly explains this apparent immaturity of the M-like cells in the hITM. Further, in contrast to enterocytes or M-like cells, the secretory-like cell cluster showed a non-canonical gene expression profile lacking the expression of markers characterizing typical subtypes of secretory cells in the small intestine^{23,26}. Among them are *CHGA* (Chromogranin A) and *NEUROG3* (Neurogenin 3) expressed by enteroendocrine cells, *DEFA5* (Defensin Alpha 5) and *REG3A* (Regenerating Family Member 3 Alpha)

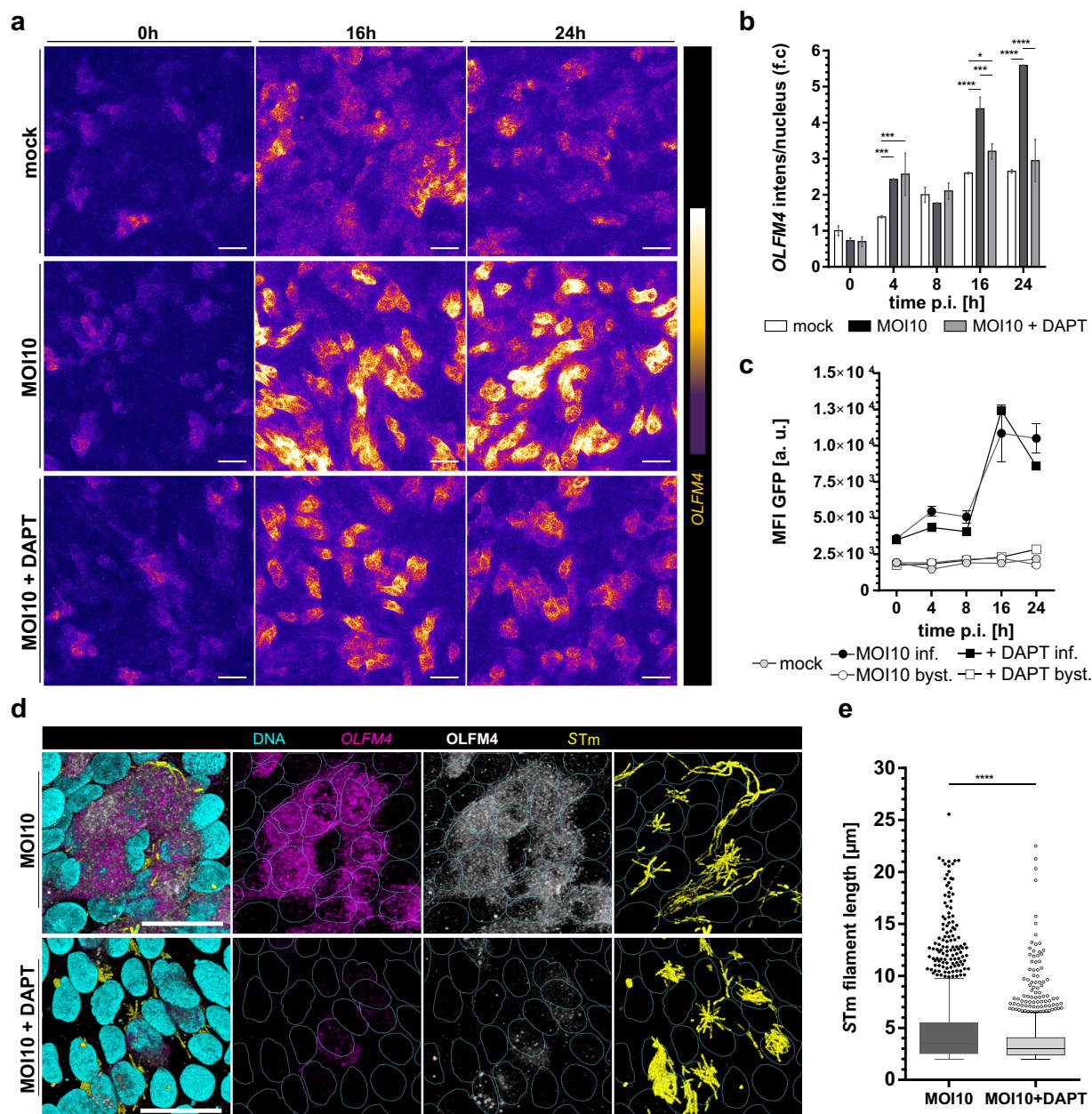


Figure 4. OLFM4 induction in STm-infected hITM depends on NOTCH signaling. **Aa** Representative fluorescent images of uninfected (mock) and STm-infected models, either treated (MOI 10 + DAPT) or not (MOI 10) with the NOTCH-specific γ -secretase-inhibitor DAPT at 0 h, 8 h, and 24 h post infection. OLFM4 mRNA levels were detected with HCR-FISH and visualized as intensity range in maximum projection images ($n = 2$). Scale bar: 20 μ m. **b** Quantification of OLFM4 mRNA intensity per nucleus. OLFM4 mRNA-specific signal intensity was measured in fluorescent images. The mean intensity value was normalized to the number of nuclei and is shown as fold change (f.c.) ($n = 2$). Significance was calculated comparing the conditions within each time point via ordinary two-way ANOVA with statistically significant differences and Tukey's multiple comparisons test with ****= $p \leq 0.0001$, ***= $p \leq 0.001$, **= $p \leq 0.01$, *= $p \leq 0.05$. Insignificant p-values are not displayed. **c** MFI of GFP per infected and uninfected IEC of mock- or STm-infected models, treated (+ DAPT) or not (MOI 10) with the NOTCH-specific γ -secretase-inhibitor DAPT at 0 h, 4 h, 8 h, 16 h, and 24 h post infection ($n = 3$ for mock and MOI 10, $n = 1$ for MOI 10 + DAPT; all technical duplicates). **d** 3D projection of representative images of HCR-FISH analyses at 24 h p. i. showing the expression of OLFM4 mRNA and protein in STm-infected cells in the untreated hITM (MOI 10) compared to DAPT-treated models (MOI 10 + DAPT). GFP expressing STm are shown in yellow, OLFM4 mRNA signals in magenta, OLFM4 protein expression in white and nuclear counterstaining with DAPI in cyan ($n = 2$). Scale bar: 20 μ m. **e** Bar diagram depicting STm filament lengths in the infected untreated hITM (MOI 10) compared to the DAPT-treated hITM infected with STm (MOI 10 + DAPT) at 24 h p.i. Filament length was determined in fluorescent images by automated filament recognition via Imaris; filaments with $< 2 \mu$ m were excluded from the analysis ($n = 2$). Data are presented as box-plot with Tukey Whiskers and significance was calculated by Mann-Whitney test with ****= $p \leq 0.0001$; two tailed. OLFM4: Olfactomedin 4, STm: *Salmonella* Typhimurium, MOI: multiplicity of infection, p.i.: post infection, hITM: human intestinal tissue model, IEC: intestinal epithelial cell, MFI: median fluorescence intensity.

expressed by Paneth cells, *TFF3* (Trefoil Factor 3) and *SPINK4* (Serine Peptidase Inhibitor Kazal Type 4) expressed by mature goblet cells. Instead, we could define the secretory-like cell cluster based on non-canonical genes including *F3* or *RAB3B* expressed by enteroendocrine cells^{30,31}, *DHSR9* or *TFF1* associated with goblet cell identity^{24,29,32}, according to the online intestinal cell atlas²³. In general, the gene expression profile of the secretory-like cell cluster does not show specificity for a secretory subtype, but rather a mixture of gene expression patterns of all secretory cells. This suggests that we possibly generated a precursor of the secretory lineage by our applied differentiation protocol. However, whether differentiated secretory subtypes derive from a specific precursor has not yet been fully proven and therefore requires further investigation, as shown by the non-canonical WNT regulation of Paneth and EEC development without goblet cell differentiation⁴⁴. In this context, our hITM could represent a suitable *in vitro* platform enabling secretory lineage differentiation studies involving a bioartificial cell niche represented by the native ECM component. In addition to the secretory-like cell cluster, we defined a second, HLA-G cell cluster based on a non-canonical gene expression profile, predominantly characterized by elevated expression levels of the *HLA-G* gene, which encodes an immunomodulatory molecule, by intestinal epithelial cells^{45,46}. The data confirm that the epithelium of the hITM contains key cell types of the native tissue.

To evaluate the hITM as a potential host model for infection experiments with enteric pathogens, we centered on the well-established model pathogen STm. Infection of our hITM recapitulated (1) STm adherence to the brush border, (2) actin remodeling, resulting in cell membrane protrusion and formation of the characteristic “donut” shape surrounding the bacteria, (3) STm encapsulation by the membrane, leading to membrane perturbations, (4) endocytosis of STm into the cytoplasm, and (5) restoration of the F-actin cytoskeleton^{33,47}. In contrast to the conventional ruffle-induced invasion process typically observed with cell line-based models^{48,49}, our data support a recently proposed alternative STm invasion mechanism referred to as discrete invasion (DI)⁴⁸. Specifically, using a mouse model, these authors showed that

STm enter absorptive epithelial cells via a Rho GTPase-independent process, which does not entail actin ruffling. The hITM thus lends itself for mechanistic studies of the DI-induced invasion process of STm.

Following invasion, enteric pathogens often transmigrate to the basolateral side of the epithelium by hijacking host cellular transport machinery^{50–52}. Indeed, we observed time-dependent STm transmigration from the apical membrane toward the basolateral region of the epithelium. Future experiments may address whether these processes are mediated by *Salmonella* pathogenicity island 2 (SPI-2) T3SS effector proteins, as recently suggested⁵³. Transmigration was accompanied by morphological changes of the intracellular bacteria. In the early phases of infection (0–8 h p.i.), STm exhibited its typical rod-shaped morphology; however, adopted a more elongated shape at the later stages. This culminated at 24 h p.i., when STm formed multinucleated, elongated filaments. Bacterial filamentation can result from perturbed cell division and has been observed in a variety of species^{54,55}. Several *Salmonella* enterica serovars are known to form this filamentous morphology extracellularly, in response to environmental factors, such as osmotic stress or temperature variations^{56,57}. However, the significance of intracellular filamentous STm is currently poorly understood^{58–61}. Of note, we are confident that filamentous STm inside IECs are not just technical artifacts of our infection protocol. For example, all our models were exposed to the same gentamicin concentration, whereas STm filamentation was exclusive to NOTCH-proficient cells yet absent when NOTCH signaling was inhibited.

We also measured the host responses to STm infection of the hITM. Among others, we observed an increase in *OLFM4* and *MUC1* expression following infection. The increased *MUC1* expression is consistent with a recently reported host defense response against enteric pathogens⁶². In contrast, *OLFM4* is predominantly expressed by intestinal stem cells^{23,63}, but was upregulated in the gastric mucosa of patients with *Helicobacter pylori*⁶⁴, in children infected with *Staphylococcus aureus*^{65,66}, in *Lawsonia intracellularis* infected intestinal porcine crypts⁶⁷, and linked to the infection of the oral

mucosa with *Porphyromonas gingivalis*⁶⁸. Our further characterization revealed the elevated expression of *OLFM4* to be triggered by NOTCH signaling in consistency with former reports⁶⁹. Importantly, *OLFM4* expression did not correlate with the levels of *LGR5* mRNA, suggesting the upregulation of *OLFM4* as a potential novel host cell response to STm infection, independent of the stem cell context. Previous STm infection studies that were coupled to transcriptomics, were often based on immortalized cell-line models,^{37,70} providing a possible explanation for why this aspect of the epithelial response to STm may have previously gone unnoticed. Consistent with recent studies, which listed increased *OLFM4* expression in STm-infected iPSC derived organoids^{71,72}, our study demonstrated that *OLFM4* is upregulated in individual infected epithelial cells during STm infection. Of note, *OLFM4* expression was found upregulated in IBD patient-derived intestinal epithelial cells^{73,74}, suggesting this to be a genuine inflammation-induced response of human primary intestinal tissues. Together, our present data imply a new role of *OLFM4* in *Salmonella* infection. Yet further analysis is needed to evaluate the effect of *OLFM4* on infection outcome and thus, to distinguish between a potential STm virulence versus host defense mechanism.

Outlook

Taken altogether, the here presented hITM represents a valuable tool for preclinical infection research, but still leaves room for future improvements. Although composed of several cellular entities of the native intestinal epithelium, our model does not yet include all mature intestinal cell types present *in vivo*. For example, we could not identify mature canonical goblet cells⁷⁵, mature Paneth cells⁷⁶, enteroendocrine cells (EEC; including I-, K-, L-, M-, N-, D-, enterochromaffin cells),⁷⁷ or Tuft cells⁷⁸. Future studies will therefore focus on increasing the cellular complexity of the hITM. For example, refinements of the differentiation protocol could increase cellular diversity, e.g. by the administration of a MAP kinase inhibitor and/or bone morphogenesis protein-4 (BMP4), possibly triggering the differentiation of the enteroid-containing ISCs in the hITM toward a mature

EEC phenotype^{79,80}. The inclusion of additional cell types would also be relevant to assess the role of stromal, endothelial, and/or immune cells in STm infections. In addition, substituting the porcine matrix with a human matrix would bring the hITM even closer to the human situation.

Material & methods

Animal handling and biological matrix preparation

Animal research was performed according to the German law and institutional guidelines approved by the Ethics Committee of the District of Unterfranken, Würzburg, Germany (approval number 55.2-2532-2-256). The biological matrix (SIS; small intestinal submucosa) was prepared from jejunal segments explanted from young pigs (age: 6–8 weeks; weight: ~20 kg; provided by Niedermayer, Dettelbach, Germany). After explantation of jejunal segments, chemical decellularization was performed according to previously published protocols^{81,82}.

Human tissue

Human jejunal biopsies used for crypt isolation were obtained from obese patients undergoing gastric bypass surgery at the University Hospital Würzburg, surgery unit of PD Dr. med. C. Jurowich. Informed written consent was obtained beforehand. The use of human tissue was approved by the Institutional Ethics Committee on Human Research of the Julius-Maximilians University Würzburg (approval number: 280/18-sc).

Organoid culture

Small intestinal organoids were established from human tissue biopsies as previously described^{7,16,83}. Briefly, after isolating the intestinal crypts from tissue biopsies, cells were diluted in ice cold Matrigel®, mixed in a 1:1 ratio with an expansion medium, and were seeded as 10–50 µl drops into 24 well tissue culture plates. After solidification of the Matrigel® drops at 37°C, cells were covered with 300 µl Expansion medium consisting of 75% conditioned LWRN medium (contains

Wnt-3A, R-Spondin-1, and Noggin, produced by cell-line L-WRN (ATCC)⁸⁴+25% Complex medium (Advanced DMEM F12 (Gibco) with 10 mM HEPES (Sigma Aldrich), 1× GlutaMax-I (Gibco), 1× Anti-Anti (Gibco), 1 mM N-Acetylcysteine (Sigma Aldrich), 1× N2-Supplement (Gibco), 1× B27-Supplement without vitamin A (Gibco)) supplemented with 0.05 µg/ml mEGF (Peprotech), 0.01 µM Leu-Gastrin (Sigma Aldrich), 10 µM Nicotinamide (Sigma Aldrich), 0.5 µM A83-01 (Tocris), 10 µM SB202190 (Sigma Aldrich), 0.5 µM LY2157299 (CAYMAN Chemical Company). Cells were cultured at 37°C, 95% humidity, 5% CO₂ and medium was changed every 2–3 days.

Passaging of small intestinal organoid cultures was performed every 5–6 days by enzymatic and mechanical dissociation. To this aim, the organoid-containing Matrigel® drops were collected with the Expansion medium, incubated on ice for 30 min, centrifuged at 350×g for 3 min, followed by dissociation of the pellet using 1–2 ml 1× TrypLE™ express incubated for up to 10 min at 37°C. Afterward, the pellet was gently pipetted to obtain single cells that were washed in a complex medium and subsequently reseeded in Matrigel® drop cultures with a cell density of 1000 IECs/µl. After solidification of the Matrigel® drops at 37°C, cells were covered with 300 µl Expansion medium supplemented with 10 µM Y-27632 (CAYMAN Chemical Company) and 10 µM JAG-1 (AnaSpec Inc.). After 2 days, the medium was changed to Expansion medium without Y-27632 and JAG-1.

hITM generation

The hITM model was established as recently described¹⁶ with the following modifications: 1) small intestinal organoids were washed with 1× PBS without calcium or magnesium (PBS-) and dissociated into single cells by TrypLE™ express treatment, 2) 4×10^5 cells diluted in 300 µl Expansion medium supplemented with 10 µM Y-27632 (CAYMAN Chemical Company), and 10 µM JAG-1 (AnaSpec Inc.) were seeded per 0.54 cm² into the apical compartment of a iScript™-like cell crown system with the biological SIS matrix as scaffold, 3) the basolateral compartment was filled with 900 µl Expansion medium containing 10 µM

Y-27632 (CAYMAN Chemical Company) and 10 µM JAG-1 (AnaSpec Inc.), 4) cells adhered after 2 days to the scaffold and tissue models were kept in Expansion Medium without Y27632 and JAG-2 for additional 3–4 days (= Proliferation Phase), 5) the Expansion medium was changed to Differentiation medium (25% conditioned Wnt-3A medium (produced by cell-line L-Wnt-3A (ATTC)⁸⁵+75% Complex medium supplemented with 0.5 µg/ml R-Spondin-1 (Peprotech), 0.1 µg/ml rec mNoggin (Peprotech), 0.05 µg/ml mEGF (Peprotech), 0.01 µM Leu-Gastrin (Sigma Aldrich), 0.5 µM A83-01 (Tocris), 0.5 µM LY2157299 (CAYMAN Chemical Company)) to initiate the differentiation of intestinal stem cells toward distinct cellular entities of the intestinal epithelium, and 6) the differentiation was performed for 4 days (= Differentiation Phase).⁸⁶

Salmonella enterica serovar Typhimurium culture and hITM infection

The constitutively GFP expressing the Wild-type derivative of *Salmonella* Typhimurium strain SL1344 (JVS-3858, (Papenfort et al. 2009)) was used in infection experiments. Bacteria were cultured in 5 ml Lennox broth (LB) at 37°C under constant agitation at 220 rpm (New Brunswick, Innova 44), overnight. For hITM infection, a 1:100 dilution of the overnight culture was grown to an OD of 2.0, pelleted by centrifugation (10,000×g for 5 min RT) and resuspended in a Complex medium without antibiotics to obtain the bacterial infection medium. For an MOI of 10, 4×10^8 bacteria diluted in 300 µl Complex medium were applied to the apical compartment of the hITM. The basolateral compartment was filled with 900 µl Complex medium. Subsequently, for synchronized bacterial adhesion, the tissue models were centrifuged at 250×g for 10 min at RT and incubated at 37°C, 95% humidity, 5% CO₂ for 1 h. After adhesion, the medium (apical and basolateral) was exchanged to a Complex medium containing High Gentamicin (Gibco) (50 µg/ml), and models were incubated for 30 min at 37°C, 95% humidity, 5% CO₂, in order to inactivate extracellular bacteria. Afterward, the High Gentamicin containing Complex medium was exchanged to a Low Gentamicin-Complex medium (10 µg/ml)

applied for ongoing culturing of the models at 37°C, 95% humidity, 5% CO₂ to prevent reinfection of the hITM.

Model dissociation for analyses of infection characteristics

For analyses of the hITM 0 – 24 h post infection, supernatants of the apical and basolateral compartments were discarded, followed by washing the models with 1× PBS+1 mM EDTA (ThermoFisher) and incubation with Accutase (Gibco), added to both compartments, incubating for 10 min at 37°C. To detach the cells from the scaffold, the Accutase suspension in the apical compartment was vigorously resuspended and transferred to a 2 ml reaction tube. The Accutase solution of the basolateral compartment was discarded and the SIS scaffold was transferred to the 2 ml reaction tube containing the Accutase solution harvested from the apical site of the model with subsequent incubation on a shaker for 10 min, 37°C at 1000 rpm. After careful resuspension using a 1 ml pipet and 10 min incubation at RT to allow settling of the cells by gravitation, the scaffold was removed. Next, the cells were centrifuged at 500×g for 3 min, RT and the supernatant was discarded. Afterward, the pellet was washed twice with 1× PBS-. Finally, cells were resuspended in 1× PBS- and stored on ice for further analysis. Before flow cytometry and Drop-seq were performed, the cells were filtered through a 40 µm Strainer (Miltenyi).

Infection rates were determined by flow cytometry performed via BD FACS Aria III (BD Biosciences) gating for STm-expressed GFP. To this aim, single-cell suspensions were filtered through a 30 µm cell strainer (Miltenyi Biontech) and a 85 µm nozzle was applied for flow cytometric procedure. Flow cytometric laser and filter settings were adjusted on unstained and uninfected cells and at least 10,000 cells were analyzed. Cells were gated based on SSC-A and FSC-A, followed by doublet discrimination via SSC-A/SSC-H and FSC-A/FSC-H. Uninfected and bystander cells were determined as GFP(-) PerCP-Cy5-5-A(-), including a small population of GFP(+)/PerCP-Cy5-5-A(+) cells. Infected cells were determined as GFP(+)/PerCP-Cy5-5-A(-) cells.

Cell hashing and dropseq

Single cells were dissociated from the hITM as described. The cells of two different models were hashtagged with TotalSeq-A antibodies (Biolegend) following the manufacturer's protocol for TotalSeqTM-A antibodies and cell hashing with 10× Single Cell 3' Reagent kit v3.1 (10× Genomics). Approximately 400,000 cells per sample were resuspended in 100 µl Cell Staining Buffer (Biolegend) and 5 µl Human TruStain FcXTM FcBlocking (Biolegend) reagent were added. For the blocking reaction, the cells were kept at 4°C for 10 min. 1 µg of TotalSeqTM-Antibody was added to each sample, followed by 30-minutes incubation at 4°C. Afterward, cells were washed three times with 1 ml Cell Staining Buffer and spun down for 5 min at 350×g and 4°C. Finally, the cells were resuspended in an appropriate volume of PBS- and passed through a 40 µm cell strainer (FlowmiTM Cell Strainer, Merck). Cells were counted in a Neubauer Hemacytometer (Marienfeld) and concentration was adjusted to 1000 cells/µl with PBS-. The hashtagged cells were pooled equally and ~ 20,000 cells were loaded in the ChromiumTM Controller. The machine creates Gel Bead-In-Emulsions (GEMs) to separate single cells into a nanoliter compartment together with an individual barcode. Reverse transcription, cDNA amplification, and the construction of gene expression libraries were performed using the 10× Single Cell 3' reaction kit v3.1 (10× Genomics). Incubation and amplification steps were carried out using a SimpliAmp Thermal Cycler (ThermoFisher). Library quantification and quality control was observed using a QubitTM 4.0 Fluorometer (ThermoFisher) and a 2100 Bioanalyzer with High Sensitivity DNA kit (Agilent). Sequencing was performed on a NextSeq 500 sequencer (Illumina).

Bioinformatic analysis

FASTQ files were aligned and counted using the CellRanger count pipeline against the GRCh38 human genome reference as well as the TotalSeqA Hashtags 1 and 2. The count matrix was imported into R for analysis using the Seurat

framework. All R scripts used in the analysis process are available at <https://github.com/saliba-lab/tissue-model-human-intestine.git>. Briefly, the count matrix was split between counts for hashtags and gene expression. Hashtags were assigned by using count thresholds to distinguish replicates (Hashtag 1, 30; Hashtag 2, 50). Unstained (negative) and double positive (doublet) cells were removed. Gene expression counts were normalized ($\log_{10}(\text{CP10k} + 1)$), 5000 highly variable genes were selected, and 45 principle components (PCs) were computed for UMAP projection, SNN graph ($k = 10$, $\text{type} = \text{rank}$), and leiden clustering ($\text{resolution_parameter} = 1.2$, $\text{n_iterations} = 5$). Differential gene expression was assessed using `scran:findMarkers(block=Replicate, pval.type=some)`. Visualizations were created with custom code using the `ggplot2`, `dplyr`, `tidyr`, and `phatmap` packages. The versions of all installed packages are specified in conda YML files in the GitHub repository (`envs/default.yml`).

Histological analyses

For histological analyses, tissue models were washed with $1\times$ PBS–before fixation in 4% PFA, 2 h at RT. Afterward, tissue models were washed with $1\times$ PBS–, covered with 70% EtOH and stored in the dark at 4°C until further processing.

Paraffin embedding was performed using a Microm STP 120 (ThermoFisher). Briefly, samples were first dehydrated by incubating in an ascending row of H_2O , 50% EtOH, 75% EtOH, 90% EtOH, 2-Propanol and Xylol with subsequent incubation in liquid paraffin.

Alcian blue staining was performed on $5\ \mu\text{m}$ sections of paraffin embedded samples, cut with a Sliding Microtome RM 2255 (Leica). Tissue slices were deparaffinized at 60°C for 1 h followed by rehydration of the sections by incubating them in a descending row of Xylol, 90% EtOH, 75% EtOH, 50% EtOH, and H_2O . Afterward, the sections were incubated in 3% acetic acid, 1% Alcian blue (Morphisto), and nuclear fast red solution (Morphisto) according to HADDOCK, 1948 before the samples were dehydrated and embedded in Entellan (Merck).

For immunohistological (IHC) analysis, paraffin-sections were dewaxed and rehydrated. After

rehydration, heat-mediated antigen retrieval was performed for 20 min at 95°C in $1\times$ citrate-buffer (Sigma). Following this, sections were permeabilized with 0.2% Triton X-100 (BioRad) in PBS–, blocked with 5% donkey serum in $1\times$ PBS–containing 0.5% Tween 20 (PBS-T) and finally incubated in PBS-T with primary antibodies (MUC-1 (Abcam, ab109185), MUC-2 (Abcam, ab76774), VIL-1 (Santa Cruz, sc7672), pan-Cytokeratin (DAKO, Z0622)) overnight at 4°C . After washing the samples twice with PBS-T on the next day, secondary antibodies (Donkey anti-rabbit AF647, donkey anti-goat AF555 (Invitrogen)) were applied for 2 h at RT diluted in PBS-T. Stained samples were washed with PBS-T and embedded in Fluoromount G containing DAPI (Invitrogen) for nuclei staining.

For whole mount staining, fixed models were disassembled, transferred to a well plate and then permeabilized using 0.2% Triton X-100 (BioRad). After washing with PBS-T, unspecific-binding sites were blocked by incubation with 5% donkey serum (Biozol) diluted in PBS-T for 30 min at RT before incubation with primary antibodies ((ZO-1 (Ptlab 21,773), OCLN (ThermoFisher 33–1500), OLFM4 (Cell Signaling D1E4M)) diluted in PBS-T overnight at 4°C . After washing twice with PBS-T the next day, secondary antibodies (Donkey anti-rabbit AF647, donkey anti-mouse AF555 (Invitrogen)) diluted in PBS-T were applied for 2 h, RT. Models were washed once in PBS-T, incubated with Phalloidin (Abcam ab176756, ab176759) and/or DAPI (ThermoFisher) diluted in PBS-T for 20 min at RT and washed twice with PBS-T. Finally, models were embedded in Fluoromount G (Invitrogen).

Electron microscopy

For scanning electron microscopy (SEM) and transmission-electron microscopy (TEM), tissue models were first washed with $1\times$ PBS–before fixation overnight at 4°C in 0.1 M phosphate buffer pH 7.4 (9.46 g/L Na_2HPO_4 , 9,078 g/L KH_2PO_4 in ddH $_2\text{O}$) containing 6.25% glutaraldehyde (VWR). Fixed samples were then washed five times in 0.1 M phosphate buffer before sample preparation for SEM/TEM and imaging that was carried out in collaboration with Prof. Stigloher from the

Biocenter Imaging Core Facility, University of Würzburg. For TEM, the samples were washed in 50 mM Cacodylate Buffer (pH 7.2, Roth) and further fixed with 2% buffered OsO₄ (ScienceServices). They were then contrasted with 0.5% watery Uranyl Acetate (Merck) and finally embedded in Epon (Serva) after EtOH-based dehydration. Cross-sections with 65 nm thickness were generated from the Epon embedded samples and contrasted with 2% Uranyl Acetate in EtOH and Reynolds stain⁸⁷. The TEM imaging was performed on a JEM-2100 (JEOL Ltd.) with 200 kV using a TVIPS TemCam F416 for image registration. For SEM, the samples were dehydrated with acetone and further dried via critical point drying. Before imaging 10–20 nm gold/palladium (80/20) were applied on the sample in an argon bath using a BAL-TEC SCD 005 Sputter Coater (Leica Mikrosysteme). The SEM imaging was performed on a JEOL JSM-7500F scanning electron microscope (JEOL Ltd.).

Quantitative real-time PCR (qRT-PCR)

For RNA isolation, tissue models were washed with PBS- and directly frozen at –80°C. RNA was isolated using the RNeasy Micro Kit (Quiagen) according to the manufacturer's protocol. Afterward, cDNA synthesis was performed with iScript™ cDNA Synthesis Kit (BioRad) following the manufacturer's instructions within a thermocycler (Sigma) with 5 min at 25°C, 30 min at 42°C, 5 min at 95°C, and hold at 4°C. RT-qPCR was performed with 25 ng cDNA using the EvaGreen® Supermix (Bio-Rad) and a CFX 96 Touch™ Real-Time PCR Detection 395 System (Bio-Rad). Plates with technical duplicates were analyzed with the following reaction condition: 40 cycles of 95°C for 10 sec, 60°C 10 sec, 72°C 30 sec. The following exon-spanning primer pair sequences were used: *OLFM4* (P1: 5'-ACTGTCCGAATTGACATCATGG-3', P2: 5'-TTCTGAGCTTCCACCAAACTC-3'⁸⁸), *EF1a* (P1: 5'-AGGTGATTATCCTGAACCATCC-3', P2: 5'-AAAGGTGGATAGTCTGAGAAG C-3'¹⁶), (P1: 5'-GCAGCATTACCTGCTCTACGT T-3', P2: 5'-GCTTGATAAGCTGATGCTGTAA TTT-3'), (P1: 5'-CCGCTACTGGTGTAAATGAT GG-3', P2: 5'-CATCAGCGATGTTATCTTGC

AG-3'), (P1: 5'-AGCTTCTACTCTGGTGACACA A-3', P2: 5'-GGTGGCTGGGAATTGAGA-3'), (P1: 5'-TCACCTCCCCAGGCCCTTC-3', P2: 5'-TGTTCACTGCTGCGATGACCCC-3').

Human *EF1a* was used as a reference gene. Fold changes of gene expression were calculated using the $\Delta\Delta CT$ method.

High-throughput qPCR barrier chip

Gene expression analysis via a high-throughput qPCR barrier chip was performed as previously reported^{89–92}. In detail, 20 μ l cDNA was produced from 250 ng RNA using the High Capacity cDNA Reverse Transcriptase Kit (Thermo Fisher Scientific). After preamplification of the targets, the high-throughput qPCR chip was performed with the preamplified cDNA in 96 \times 96 chips using the Biomark™ system (Fluidigm®).

HCR-FISH

DNA probes for HCR-FISH were designed as previously described⁹³. 25-nucleotide (nt) sequences of each gene were extracted. One probe consists of a pair of two 25-nt long oligos (25-nt encoding region, 2-nt spacer, and 18-nt initiator region) separated by a 2-nt gap. The oligo pairs were selected to have a T_m difference of <5°C. In addition, probe sequences were required to have a GC content within the 40–60% range. The NCBI database was used to look up mRNA sequences. Any probe sequence that contained five or more consecutive bases of the same kind was dropped. To ensure specificity, an NCBI BLAST query was run on each probe against the human transcriptome. BLAST hits on sequences other than the target gene with a 15-nt match were considered off-targets. For each gene, eight encoding probe pairs were designed. Read-out amplifiers B3 with AF546 fluorophores were ordered from Molecular Instruments.

HCR-FISH staining was performed with a HCR-FISH kit (Molecular Instruments) according to the manufacturer's protocol with minor modifications. Briefly, after fixation, the samples were permeabilized in 70% EtOH, washed once with 1 \times PBS-T and once with 5 \times saline sodium citrate buffer (Sigma) with 0.5% Tween

(BioRad) (SSC-T). For detection, the samples were equilibrated with hybridization buffer and 5 pmol of the detection probe pool set was added. After incubation for 12 h at 37°C, samples were washed with Probe wash buffer at 37°C followed by washing with 5× SSC-T. For amplification, samples were equilibrated with the amplification buffer and incubated for 16 h at RT with 30 pmol of the amplification hairpin solution (AlexaFluor 546). The samples were washed with 5× SSC-T, stained with DAPI (ThermoFisher) diluted in PBS-T. Finally, models were embedded in Fluoromount G (Invitrogen).

For HCR-FlowFISH, dissociated single cells were fixed in 4% PFA and permeabilized with 70% EtOH. The cells were washed with 1× PBS-T and with 5× SSC-T. Afterward, 4×10^5 cells were equilibrated in hybridization buffer, 5 pmol of the detection probe pool set were added and incubated for 12 h at 37°C. After washing with Probe wash buffer and 5×-SSC-T, the cells were equilibrated in the amplification buffer followed by incubation with 30 pmol of the amplification hairpin solution (AlexaFluor 546) for 16 h at RT. Cells were washed using 5× SSC-T with subsequent dilution in 1× PBS- and flow cytometric analysis on a BD FACS Aria III (BD Biosciences). Cells (uninfected, bystander, or infected) were separated into OLFM4(+) and OLFM4(-) based on the AlexaFluor 546 signal. Gates were set discriminating between uninfected and unstained (no detection probes) cells.

Imaging

Imaging was performed with the Keyence B×810 widefield microscope (Keyence), the Leica SP8 confocal microscope (Leica), the Scanning Electron Microscope JSM-7500F (JEOL), and the Transmission Electron Microscope JEM-2100 (JEOL). The representative images were processed with Fiji (v1.51s), and 3D modeling was generated by LasX 3D Visualization.

Cell height measurement

Cell height measurements were performed on cross-section views of z-stack confocal images

representative of whole tissue samples. Briefly, a defined grid of 9×9 fields was applied on the field of view (FOV). Cell height was determined by measuring the distance between the apical and the basolateral F-actin signal of individual cells located at the cross points of the grid lines. The cell height measurements were performed via Fiji (v1.51s).

Bacterial migration measurement

For the measurement of bacterial migration within the hITM, an automated batch analysis was performed with IMARIS (v8.4.2) on representative z-stack images in 3D projection. In a first step, the threshold determining the apical F-actin signal was set. Secondly, the centers of STm-expressing GFP signals were defined, and bacterial migration was determined as distance between the defined GFP spot and the apical F-actin signal.

OLFM4 intensity measurement

OLFM4 intensity was determined with Fiji (v1.51s) as follows: 1) z-stacks of images representative of the whole hITM were projected as the sum of all stacks, 2) the mean OLFM4 HCR-FISH signal intensity in the FOV was measured, 3) the number of nuclei per FOV were determined. The OLFM4 intensity was calculated as $OLFM4_{int} = \frac{OLFM4_{meanintensity}}{numberofnuclei}$.

STm filament length

Filament lengths were determined in whole tissue samples using the Imaris software (v8.4.2) as follows: 1) regions with GFP signals were identified and determined as volumes, 2) the pixel intensity of the GFP signal outside of the defined volumes was set to zero, 3) the inbuilt filament tool was applied in the FOV to identify filaments with 0.5 μm diameter and branching points at a filament length of $>2 \mu\text{m}$ (= minimal length of one individual STm). Identified filaments with lengths $<2 \mu\text{m}$ were not considered and excluded.

Statistical analysis

Statistical analysis was performed via GraphPad Prism (v6.02) with unpaired t-test, ordinary one-

way ANOVA with Tukey's multiple comparison tests, two-ANOVA with Tukey's multiple comparison tests, and Mann-Whitney-U test.

Acknowledgments

We thank S. Reichardt, M. Krafft, and E. Reitenbach for their excellent technical support and assistance; C. Stigloher, C. Gehrig-Höhn, and D. Bunsen for the excellent support during SEM and TEM preparation and imaging; M. Heckmann and C. Werner for kindly provision of IMARIS. A. Gerhartl and A. Brachner for their support in high-throughput qPCR barrier chip measurement; Sara Giddins for editorial support.









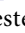


Disclosure statement

No potential conflict of interest was reported by the authors.

Funding

The work was supported by the Deutsche Forschungsgemeinschaft (DFG) [270563345]. in the context of the GRK 2157. Furthermore, the DFG funded the SEM (JEOL JSM-7500F) [218894895] and the TEM (JEOL JEM 2100) [218894163]. T.D, A.-E.S., and O.D. thanks DFG for funding through GRK2157. A.-E.S. thanks DFG funding SFB1583 (DECIDE; Project B05). A.-E.S. thank the Single Cell Center Würzburg for support. T.K. thanks DFG funding via SFB1525 (Cardio-Immuno Interface: PS2 Project).

ORCID

Thomas Däullary  <http://orcid.org/0000-0001-5113-3768>
 Fabian Imdahl  <http://orcid.org/0000-0002-3796-2946>
 Oliver Dietrich  <http://orcid.org/0000-0002-4776-8960>
 Tobias Krammer  <http://orcid.org/0000-0002-7638-9476>
 Christina Fey  <http://orcid.org/0000-0001-6860-8184>
 Winfried Neuhaus  <http://orcid.org/0000-0002-6552-7183>
 Marco Metzger  <http://orcid.org/0000-0003-2053-9401>
 Jörg Vogel  <http://orcid.org/0000-0003-2220-1404>
 Alexander J. Westermann  <http://orcid.org/0000-0003-3236-0169>
 Antoine-Emmanuel Saliba  <http://orcid.org/0000-0001-8539-2784>
 Daniela Zdziebło  <http://orcid.org/0000-0002-6606-2445>

Data availability statement

Repository: <https://www.ncbi.nlm.nih.gov/geo/> Accession number: GSE217976

References

1. Kolling G, Wu M, Guerrant RL. Enteric pathogens through life stages. *Front Cell Infect Microbiol.* 2012;2:114. doi:10.3389/fcimb.2012.00114.
2. McCracken KW, Catá EM, Crawford CM, Sinagoga KL, Schumacher M, Rockich BE, Tsai Y-H, Mayhew CN, Spence JR, Zavros Y, et al. Modelling human development and disease in pluripotent stem-cell-derived gastric organoids. *Nat.* 2014;516(7531):400–404. 20145167531. doi:10.1038/nature13863.
3. McCracken KW, Howell JC, Wells JM, Spence JR. Generating human intestinal tissue from pluripotent stem cells in vitro. *Nat Protoc.* 2011;6(12):1920–1928. doi:10.1038/nprot.2011.410.
4. Miura S, Suzuki A. Generation of mouse and human organoid-forming intestinal progenitor cells by direct lineage reprogramming. *Cell Stem Cell.* 2017;21(4):456–471.e5. doi:10.1016/j.stem.2017.08.020.
5. Spence JR, Mayhew CN, Rankin SA, Kuhar MF, Vallance JE, Tolle K, Hoskins EE, Kalinichenko VV, Wells SI, Zorn AM, et al. Directed differentiation of human pluripotent stem cells into intestinal tissue in vitro. *Nat.* 2010;470(7332):105–109. 2010 4707332. doi:10.1038/nature09691.
6. Miyoshi H, Stappenbeck TS. In vitro expansion and genetic modification of gastrointestinal stem cells in spheroid culture. *Nat Protoc.* 2013;8(12):2471–2482. doi:10.1038/nprot.2013.153.
7. Sato T, Vries RG, Snippert HJ, van de Wetering M, Barker N, Stange DE, van Es JH, Abo A, Kujala P, Peters PJ, et al. Single Lgr5 stem cells build crypt-villus structures in vitro without a mesenchymal niche. *Nature.* 2009;459(7244):262–265. doi:10.1038/nature07935.
8. Aguilar C, Alves da Silva M, Saraiva M, Neyazi M, Olsson IAS, Bartfeld S. Organoids as host models for infection biology – a review of methods. *Exp Mol Med.* 2021 2021310;53(10):1471–1482. doi:10.1038/s12276-021-00629-4.
9. Aguilar C, Pauzuolis M, Pompaiah M, Vafadarnejad E, Arampatzi P, Fischer M, Narres D, Neyazi M, Kayisoglu Ö, Sell T, et al. Helicobacter pylori shows tropism to gastric differentiated pit cells dependent on urea chemotaxis. *Nat Commun.* 2022;13(1):5878. doi:10.1038/s41467-022-33165-4.
10. Pinto N, et al. Markers and methods to study adult midgut stem cells. *Methods Mol Biol.* 2018;1842:123–137.
11. Saxena K, Blutt SE, Ettayebi K, Zeng X-L, Broughman JR, Crawford SE, Karandikar UC, Sastri NP, Conner ME, Opekun AR, et al. Human intestinal enteroids: a new model to study human rotavirus infection, host restriction, and pathophysiology. *J Virol.* 2016;90(1):43–56. doi:10.1128/JVI.01930-15.
12. Holly MK, Smith JG, Pfeiffer JK. Adenovirus infection of human enteroids reveals interferon sensitivity and

- preferential infection of goblet cells. *J Virol.* 2018;92(9). doi:10.1128/JVI.00250-18.
13. Han Y, Yang L, Lacko LA, Chen S. Human organoid models to study SARS-CoV-2 infection. *Nat Methods.* 2022 194 2022;19(4):418–428. doi:10.1038/s41592-022-01453-y.
 14. Foulke-Abel J, In J, Kovbasnjuk O, Zachos NC, Ettayebi K, Blutt SE, Hyser JM, Zeng X-L, Crawford SE, Broughman JR, et al. Human enteroids as an ex-vivo model of host–pathogen interactions in the gastrointestinal tract. *Exp Biol Med (Maywood).* 2014;239(9):1124–1134. doi:10.1177/1535370214529398.
 15. Nickerson KP, Llanos-Chea A, Ingano L, Serena G, Miranda-Ribera A, Perlman M, Lima R, Szein MB, Fasano A, Senger S, et al. A versatile human intestinal organoid-derived epithelial monolayer model for the study of enteric pathogens. *Microbiol Spectr.* 2021;9(1). doi:10.1128/Spectrum.00003-21.
 16. Schweinlin M, Wilhelm S, Schwedhelm I, Hansmann J, Rietscher R, Jurowich C, Walles H, Metzger M. Development of an advanced primary human in vitro model of the small intestine. *Tissue Eng Part C Methods.* 2016;22(9):873–883. doi:10.1089/ten.tec.2016.0101.
 17. Crowe P, Marsh M. Morphometric analysis of small intestinal mucosa. IV. determining cell volumes. *Virchows Arch A Pathol Anat Histopathol.* 1993;422(6):459–466. doi:10.1007/BF01606454.
 18. Srinivasan B, Kolli AR, Esch MB, Abaci HE, Shuler ML, Hickman JJ. TEER measurement techniques for in vitro barrier model systems. *J Lab Autom.* 2015;20(2):107–126. doi:10.1177/2211068214561025.
 19. Owen RL, Jones AL. Epithelial cell specialization within human peyer’s patches: an ultrastructural study of intestinal lymphoid follicles. *Gastroenterology.* 1974;66(2):189–203. doi:10.1016/S0016-5085(74)80102-2.
 20. Grondin JA, Kwon YH, Far PM, Haq S, Khan WI. Mucins in intestinal mucosal defense and inflammation: learning from clinical and experimental studies. *Front Immunol.* 2020;11:2054. doi:10.3389/fimmu.2020.02054.
 21. Revenu C, Ubelmann F, Hurbain I, El-Marjou F, Dingli F, Loew D, Delacour D, Gilet J, Brot-Laroche E, Rivero F, et al. A highlights from MBoC selection: a new role for the architecture of microvillar actin bundles in apical retention of membrane proteins. *Mol Biol Cell.* 2012;23(2):324. doi:10.1091/mbc.e11-09-0765.
 22. Khurana S, George SP. Regulation of cell structure and function by actin-binding proteins: villin’s perspective. *FEBS Lett.* 2008;582(14):2128–2139. doi:10.1016/j.febslet.2008.02.040.
 23. Elmentaite R, Kumasaka N, Roberts K, Fleming A, Dann E, King HW, Kleshchevnikov V, Dabrowska M, Pritchard S, Bolt L, et al. Cells of the human intestinal tract mapped across space and time. *Nature.* 2021;597(7875):250–255. doi:10.1038/s41586-021-03852-1.
 24. Wang Y, Song W, Wang J, Wang T, Xiong X, Qi Z, Fu W, Yang X, Chen Y-G. Single-cell transcriptome analysis reveals differential nutrient absorption functions in human intestine. *J Exp Med.* 2020;217(2):1–15. doi:10.1084/jem.20191130.
 25. Haber AL, Biton M, Rogel N, Herbst RH, Shekhar K, Smillie C, Burgin G, Delorey TM, Howitt MR, Katz Y, et al. A single-cell survey of the small intestinal epithelium. *Nature.* 2017;551(7680):333–339. doi:10.1038/nature24489.
 26. Burclaff J, Bliton RJ, Breau KA, Ok MT, Gomez-Martinez I, Ranek JS, Bhatt AP, Purvis JE, Woosley JT, Magness ST. A proximal-to-distal survey of healthy adult human small intestine and colon epithelium by single-cell transcriptomics. *Cell Mol Gastroenterol Hepatol.* 2022;13(5):1554–1589. doi:10.1016/j.jcmgh.2022.02.007.
 27. Kimura S, Yamakami-Kimura M, Obata Y, Hase K, Kitamura H, Ohno H, Iwanaga T. Visualization of the entire differentiation process of murine M cells: suppression of their maturation in cecal patches. *Mucosal Immunol.* 2015 201483;8(3):650–660. doi:10.1038/mi.2014.99.
 28. Mabbott NA, Donaldson DS, Ohno H, Williams IR, Mahajan A. Microfold (M) cells: important immunosurveillance posts in the intestinal epithelium. *Mucosal Immunol.* 2013;6(4):666–677. doi:10.1038/mi.2013.30.
 29. Madsen J, Nielsen O, Tornøe I, Thim L, Holmskov U. Tissue localization of human trefoil factors 1, 2, and 3. *J Histochem Cytochem.* 2007;55(5):505–513. doi:10.1369/jhc.6A7100.2007.
 30. Rupnik M, Kreft M, Nothias F, Grilc S, Bobanovic LK, Johannes L, Kiauta T, Vernier P, Darchen F, Zorec R. Distinct role of Rab3A and Rab3B in secretory activity of rat melanotrophs. *Am J Physiol - Cell Physiol.* 2007;292(1):98–105. doi:10.1152/ajpcell.00005.2006.
 31. Ryu GR, Lee E, Kim JJ, Moon S-D, Ko S-H, Ahn Y-B, Song K-H. Comparison of enteroendocrine cells and pancreatic β -cells using gene expression profiling and insulin gene methylation. *PLoS One.* 2018;13(10):e0206401. doi:10.1371/journal.pone.0206401.
 32. Parikh K, Antanaviciute A, Fawcner-Corbett D, Jagielowicz M, Aulicino A, Lagerholm C, Davis S, Kinchen J, Chen HH, Alham NK, et al. Colonic epithelial cell diversity in health and inflammatory bowel disease. *Nature.* 2019;567(7746):49–55. doi:10.1038/s41586-019-0992-y.
 33. Larock DL, Chaudhary A, Miller SI. Salmonellae interactions with host processes. *Nat Rev Microbiol.* 2015 201534;13(4):191–205. doi:10.1038/nrmicro3420.
 34. Livak KJ, Schmittgen TD. Analysis of relative gene expression data using real-time quantitative PCR and the 2– $\Delta\Delta$ CT method. *Methods.* 2001;25(4):402–408. doi:10.1006/meth.2001.1262.

35. VanDussen KL, Carulli AJ, Keeley TM, Patel SR, Puthoff BJ, Magness ST, Tran IT, Maillard I, Siebel C, Kolterud Å, et al. Notch signaling modulates proliferation and differentiation of intestinal crypt base columnar stem cells. *Development*. 2012;139(3):488–497. doi:10.1242/dev.070763.
36. Odenwald MA, Turner JR. The intestinal epithelial barrier: a therapeutic target? *Nat Rev Gastroenterol Hepatol*. 2016;14(1):9–21. doi:10.1038/nrgastro.2016.169.
37. Schulte LN, Schweinlin M, Westermann AJ, Janga H, Santos SC, Appenzeller S, Walles H, Vogel J, Metzger M. An advanced human intestinal coculture model reveals compartmentalized host and pathogen strategies during salmonella infection. *MBio*. 2020;11(1). doi:10.1128/mBio.03348-19.
38. Meran L, Massie I, Campinoti S, Weston AE, Gaifulina R, Tullie L, Faull P, Orford M, Kucharska A, Baulies A, et al. Engineering transplantable jejunal mucosal grafts using patient-derived organoids from children with intestinal failure. *Nat Med*. 2020;26(10):1593–1601. doi:10.1038/s41591-020-1024-z.
39. Siddiqui KM, Chopra DP. Primary and long term epithelial cell cultures from human fetal normal colonic mucosa. *Vitro*. 1984;20(11):859–868. doi:10.1007/BF02619632.
40. Kanaya T, Sakakibara S, Jinnohara T, Hachisuka M, Tachibana N, Hidano S, Kobayashi T, Kimura S, Iwanaga T, Nakagawa T, et al. Development of intestinal M cells and follicle-associated epithelium is regulated by TRAF6-mediated NF- κ B signaling. *J Exp Med*. 2018;215(2):501–519. doi:10.1084/jem.20160659.
41. Nakamura Y, Kimura S, Hase K. M cell-dependent antigen uptake on follicle-associated epithelium for mucosal immune surveillance. *Inflamm Regen*. 2018;38(1):1–9. doi:10.1186/s41232-018-0072-y.
42. Knoop KA, Kumar N, Butler BR, Sakthivel SK, Taylor RT, Nochi T, Akiba H, Yagita H, Kiyono H, Williams IR. RANKL is necessary and sufficient to initiate development of antigen-sampling M cells in the intestinal epithelium. *J Immunol*. 2009;183(9):5738–5747. doi:10.4049/jimmunol.0901563.
43. Nagashima K, Sawa S, Nitta T, Tsutsumi M, Okamura T, Penninger JM, Nakashima T, Takayanagi H. Identification of subepithelial mesenchymal cells that induce IgA and diversify gut microbiota. *Nat Immunol*. 2017 2017186;18(6):675–682. doi:10.1038/ni.3732.
44. Böttcher A, Büttner M, Tritschler S, Sterr M, Aliluev A, Oppenländer L, Burtscher I, Sass S, Irmeler M, Beckers J, et al. Non-canonical Wnt/PCP signalling regulates intestinal stem cell lineage priming towards enteroendocrine and Paneth cell fates. *Nat Cell Biol*. 2021;23(1):23–31. doi:10.1038/s41556-020-00617-2.
45. da Costa Ferreira S, Sadissou IA, Parra RS, Feitosa MR, Neto FSL, Pretti da Cunha Tirapelli D, Ramalho LNZ, Féres O, da Rocha JJR, Donadi EA, et al. Increased HLA-G expression in tissue-infiltrating cells in inflammatory bowel diseases. *Dig Dis Sci*. 2021;66(8):2610–2618. doi:10.1007/s10620-020-06561-3.
46. Onno M, Guillaudeux T, Amiot L, Renard I, Drenou B, Hirel B, Girr M, Semana G, Le Bouteiller P, Fauchet R. The HLA-G gene is expressed at a low mRNA level in different human cells and tissues. *Hum Immunol*. 1994;41(1):79–86. doi:10.1016/0198-8859(94)90089-2.
47. Malik-Kale P, Jolly CE, Lathrop S, Winfree S, Luterbach C, Steele-Mortimer O. Salmonella – at home in the host cell. *Front Microbiol*. 2011;2:125. doi:10.3389/fmicb.2011.00125.
48. Fattinger SA, Böck D, Di Martino ML, Deuring S, Samperio Ventayol P, Ek V, Furter M, Kreibich S, Bosia F, Müller-Hauser AA, et al. Salmonella typhimurium discreet-invasion of the murine gut absorptive epithelium. *PLoS Pathog*. 2020;16(5):e1008503. doi:10.1371/journal.ppat.1008503.
49. Fattinger SA, Sellin ME, Hardt WD. Salmonella effector driven invasion of the gut epithelium: breaking in and setting the house on fire. *Curr Opin Microbiol*. 2021;64:9–18. doi:10.1016/j.mib.2021.08.007.
50. Backert S, Boehm M, Wessler S, Tegtmeier N. Transmigration route of campylobacter jejuni across polarized intestinal epithelial cells: paracellular, transcellular or both? *Cell Commun Signal*. 2013;11(1):72. doi:10.1186/1478-811X-11-72.
51. Burns JL, Griffith A, Barry JJ, Jonas M, Chi EY. Transcytosis of gastrointestinal epithelial cells by escherichia coli K1. *Pediatr Res*. 2001 2001491;49(1):30–37. doi:10.1203/00006450-200101000-00010.
52. Colonne PM, Winchell CG, Voth DE. Hijacking host cell highways: manipulation of the host actin cytoskeleton by obligate intracellular bacterial pathogens. *Front Cell Infect Microbiol*. 2016;6:107. doi:10.3389/fcimb.2016.00107.
53. Fulde M, van Vorst K, Zhang K, Westermann AJ, Busche T, Huei YC, Welitschanski K, Froh I, Pägelow D, Plendl J, et al. SPI2 T3SS effectors facilitate enterocyte apical to basolateral transmigration of Salmonella-containing vacuoles in vivo. *Gut Microbes*. 2021;13(1). doi:10.1080/19490976.2021.1973836.
54. Justice SS, Hunstad DA, Cegelski L, Hultgren SJ. Morphological plasticity as a bacterial survival strategy. *Nat Rev Microbiol*. 2008 200862;6(2):162–168. doi:10.1038/nrmicro1820.
55. Abell-King C, Costas A, Duggin IG, Söderström B, Coers J. Bacterial filamentation during urinary tract infections. *PLoS Pathog*. 2022;18(12):e1010950. doi:10.1371/journal.ppat.1010950.
56. Lensmire JM, Pratt ZL, Wong ACL, Kaspar CW. Phosphate and carbohydrate facilitate the formation of filamentous salmonella Enterica during osmotic stress. *Microbiol (United Kingdom)*. 2018;164(12):1503–1513. doi:10.1099/mic.0.000731.
57. Mattick KL, Phillips LE, Jørgensen F, Lappin-Scott HM, Humphrey TJ. Filament formation by salmonella spp.

- inoculated into liquid food matrices at refrigeration temperatures, and growth patterns when warmed. *J Food Prot.* 2003;66(2):215–219. doi:10.4315/0362-028X-66.2.215.
58. Henry T, Garcia-Del Portillo F, Gorvel JP. Identification of Salmonella functions critical for bacterial cell division within eukaryotic cells. *Mol Microbiol.* 2005;56(1):252–267. doi:10.1111/j.1365-2958.2005.04540.x.
 59. Humphrey S, MacVicar T, Stevenson A, Roberts M, Humphrey TJ, Jepson MA. SulA-induced filamentation in salmonella enterica serovar typhimurium: effects on SPI-1 expression and epithelial infection. *J Appl Microbiol.* 2011;111(1):185–196. doi:10.1111/j.1365-2672.2011.05022.x.
 60. Martínez-Lorenzo MJ, Méresse S, De Chastellier C, Gorvel JP. Unusual intracellular trafficking of Salmonella typhimurium in human melanoma cells. *Cell Microbiol.* 2001;3(6):407–416. doi:10.1046/j.1462-5822.2001.00123.x.
 61. Schuster EM, Epple MW, Glaser KM, Mihlan M, Lucht K, Zimmermann JA, Bremser A, Polyzou A, Obier N, Cabezas-Wallscheid N, et al. TFEB induces mitochondrial itaconate synthesis to suppress bacterial growth in macrophages. *Nat Metab.* 2022;4(7):856–866. doi:10.1038/s42255-022-00605-w.
 62. Dhar P, McAuley J. The role of the cell surface mucin MUC1 as a barrier to infection and regulator of inflammation. *Front Cell Infect Microbiol.* 2019;9:117. doi:10.3389/fcimb.2019.00117.
 63. van der Flier LG, Haegebarth A, Stange DE, van de Wetering M, Clevers H. OLFM4 is a robust marker for stem cells in human intestine and marks a subset of colorectal cancer cells. *Gastroenterology.* 2009;137(1):15–17. doi:10.1053/j.gastro.2009.05.035.
 64. Mannick EE, Schurr JR, Zapata A, Lentz JJ, Gastanaduy M, Cote RL, Delgado A, Correa P, Correa H. Gene expression in gastric biopsies from patients infected with helicobacter pylori. *Scand J Gastroenterol.* 2004;39(12):1192–1200. doi:10.1080/00365520410003588.
 65. Liu W, Yan M, Sugui JA, Li H, Xu C, Joo J, Kwon-Chung KJ, Coleman WG, Rodgers GP. Olfm4 deletion enhances defense against Staphylococcus aureus in chronic granulomatous disease. *J Clin Invest.* 2013;123(9):3751–3755. doi:10.1172/JCI68453.
 66. Ramilo O, Allman W, Chung W, Mejias A, Ardura M, Glaser C, Wittkowski KM, Piqueras B, Banchereau J, Palucka AK, et al. Gene expression patterns in blood leukocytes discriminate patients with acute infections. *Blood.* 2007;109(5):2066–2077. doi:10.1182/blood-2006-02-002477.
 67. Huan YW, Bengtsson RJ, MacIntyre N, Guthrie J, Finlayson H, Smith SH, Archibald AL, Ait-Ali T. Lawsonia intracellularis exploits β -catenin/wnt and notch signalling pathways during infection of intestinal crypt to alter cell homeostasis and promote cell proliferation. *PLoS One.* 2017;12(3):e0173782. doi:10.1371/journal.pone.0173782.
 68. Fitzsimonds ZR, Liu C, Stocke KS, Yakoumatos L, Shumway B, Miller DP, Artyomov MN, Bagaitkar J, Lamont RJ. Regulation of olfactomedin 4 by Porphyromonas gingivalis in a community context. *Isme J.* 2021 2021159;15(9):2627–2642. doi:10.1038/s41396-021-00956-4.
 69. Kuno R, Ito G, Kawamoto A, Hiraguri Y, Sugihara HY, Takeoka S, Nagata S, Takahashi J, Tsuchiya M, Anzai S, et al. Notch and TNF- α signaling promote cytoplasmic accumulation of OLFM4 in intestinal epithelium cells and exhibit a cell protective role in the inflamed mucosa of IBD patients. *Biochem Biophys Reports.* 2021;25:100906. doi:10.1016/j.bbrep.2020.100906.
 70. Westermann AJ, Förstner KU, Amman F, Barquist L, Chao Y, Schulte LN, Müller L, Reinhardt R, Stadler PF, Vogel J. Dual RNA-seq unveils noncoding RNA functions in host–pathogen interactions. *Nature.* 2016;529(7587):496–501. doi:10.1038/nature16547.
 71. Abuaita BH, Lawrence ALE, Berger RP, Hill DR, Huang S, Yadagiri VK, Bons B, Fields C, Wobus CE, Spence JR, et al. Comparative transcriptional profiling of the early host response to infection by typhoidal and non-typhoidal Salmonella serovars in human intestinal organoids. *PLoS Pathog.* 2021;17(10):e1009987. doi:10.1371/journal.ppat.1009987.
 72. Lawrence ALE, Abuaita BH, Berger RP, Hill DR, Huang S, Yadagiri VK, Bons B, Fields C, Wobus CE, Spence JR, et al. Salmonella enterica serovar typhimurium spi-1 and spi-2 shape the global transcriptional landscape in a human intestinal organoid model system. *MBio.* 2021;12(3). doi:10.1128/mBio.00399-21.
 73. Shinozaki S, Nakamura T, Iimura M, Kato Y, Iizuka B, Kobayashi M, Hayashi N. Upregulation of Reg 1 α and GW112 in the epithelium of inflamed colonic mucosa. *Gut.* 2001;48(5):623–629. doi:10.1136/gut.48.5.623.
 74. Gersemann M, Becker S, Nuding S, Antoni L, Ott G, Fritz P, Oue N, Yasui W, Wehkamp J, Stange EF. Olfactomedin-4 is a glycoprotein secreted into mucus in active IBD. *J Crohn's Colitis.* 2012;6(4):425–434. doi:10.1016/j.crohns.2011.09.013.
 75. Kim YS, Ho SB. Intestinal goblet cells and mucins in health and disease: recent insights and progress. *Curr Gastroenterol Rep.* 2010;12(5):319–330. doi:10.1007/s11894-010-0131-2.
 76. Clevers HC, Bevins CL. Paneth cells: maestros of the small intestinal crypts. *Annu Rev Physiol.* 2013;75(1):289–311. doi:10.1146/annurev-physiol-030212-183744.
 77. Worthington JJ, Reimann F, Gribble FM. Enteroendocrine cells-sensory sentinels of the intestinal environment and orchestrators of mucosal immunity. *Mucosal Immunol.* 2018;11(1):3–20. doi:10.1038/mi.2017.73.
 78. Gerbe F, Jay P. Intestinal tuft cells: epithelial sentinels linking luminal cues to the immune system. *Mucosal*

- Immunol. 2016;9(6):1353–1359. doi:10.1038/mi.2016.68.
79. Beumer J, Artegiani B, Post Y, Reimann F, Gribble F, Nguyen TN, Zeng H, Van den Born M, Van Es JH, Clevers H. Enteroendocrine cells switch hormone expression along the crypt-to-villus BMP signalling gradient. *Nat Cell Biol.* 2018 2018208;20(8):909–916. doi:10.1038/s41556-018-0143-y.
80. Pleguezuelos-Manzano C, Puschhof J, den Brink S, Geurts V, Beumer J, Clevers H. Establishment and culture of human intestinal organoids derived from adult stem cells. *Curr Protoc Immunol.* 2020;130(1):e106. doi:10.1002/cpim.106.
81. Jannasch M, Groeber F, Brattig NW, Unger C, Walles H, Hansmann J. Development and application of three-dimensional skin equivalents for the investigation of percutaneous worm invasion. *Exp Parasitol.* 2015;150:22–30. doi:10.1016/j.exppara.2015.01.005.
82. Pusch J, Votteler M, Göhler S, Engl J, Hampel M, Walles H, Schenke-Layland K. The physiological performance of a three-dimensional model that mimics the microenvironment of the small intestine. *Biomaterials.* 2011;32(30):7469–7478. doi:10.1016/j.biomaterials.2011.06.035.
83. Sato T, Stange DE, Ferrante M, Vries RGJ, van Es JH, van den Brink S, van Houdt WJ, Pronk A, van Gorp J, Siersema PD, et al. Long-term expansion of epithelial organoids from human colon, adenoma, adenocarcinoma, and Barrett's epithelium. *Gastroenterology.* 2011;141(5):1762–1772. doi:10.1053/j.gastro.2011.07.050.
84. VanDussen KL, Sonnek NM, Stappenbeck TS. L-WRN conditioned medium for gastrointestinal epithelial stem cell culture shows replicable batch-to-batch activity levels across multiple research teams. *Stem Cell Res.* 2019;37:101430. doi:10.1016/j.scr.2019.101430.
85. Vonk AM, van Mourik P, Ramalho AS, Silva IAL, Statia M, Kruisselbrink E, Suen SWF, Dekkers JF, Vleggaar FP, Houwen RHJ, et al. Protocol for application, standardization and validation of the forskolin-induced swelling assay in cystic fibrosis human colon organoids. *STAR Protoc.* 2020;1(1):100019. doi:10.1016/j.xpro.2020.100019.
86. Haddock NH. Alcian blue, a new phthalocyanine dyestuff. *Research; a Journal of Science and Its Applications.* 1948;1:685–689.
87. Reynolds ES. THE USE of LEAD CITRATE at HIGH pH as an ELECTRON-OPAQUE STAIN in ELECTRON MICROSCOPY. *J Cell Biol.* 1963;17(1):208. doi:10.1083/jcb.17.1.208.
88. Freire R, Ingano L, Serena G, Cetinbas M, Anselmo A, Sapone A, Sadreyev RI, Fasano A, Senger S. Human gut derived-organoids provide model to study gluten response and effects of microbiota-derived molecules in celiac disease. *Sci Rep.* 2019;9(1):1–15. doi:10.1038/s41598-019-43426-w.
89. Krasemann S, Haferkamp U, Pfefferle S, Woo MS, Heinrich F, Schweizer M, Appelt-Menzel A, Cubukova A, Barenberg J, Leu J, et al. The blood-brain barrier is dysregulated in COVID-19 and serves as a CNS entry route for SARS-CoV-2. *Stem Cell Rep.* 2022;17(2):307–320. doi:10.1016/j.stemcr.2021.12.011.
90. Lin GC, Leitgeb T, Vladetic A, Friedl H-P, Rhodes N, Rossi A, Roblegg E, Neuhaus W. Optimization of an oral mucosa in vitro model based on cell line TR146. *Tissue Barriers.* 2020;8(2):1748459. doi:10.1080/21688370.2020.1748459/SUPPL_FILE/KTIB_A_1748459_SM4220.ZIP.
91. Gerhartl A, Pracser N, Vladetic A, Hendrikx S, Friedl H-P, Neuhaus W. The pivotal role of micro-environmental cells in a human blood–brain barrier in vitro model of cerebral ischemia: functional and transcriptomic analysis. *Fluids Barriers CNS.* 2020;17(1):1–17. doi:10.1186/s12987-020-00179-3.
92. Ramme AP, Koenig L, Hasenberg T, Schwenk C, Magauer C, Faust D, Lorenz AK, Krebs A-C, Drewell C, Schirrmann K, et al. Autologous induced pluripotent stem cell-derived four-organ-chip. *Futur Sci OA.* 2019;5(8):413–2056. doi:10.2144/fsoa-2019-0065.
93. Choi HMT, Schwarzkopf M, Fornace ME, Acharya A, Artavanis G, Stegmaier J, Cunha A, Pierce NA. Third-generation in situ hybridization chain reaction: multiplexed, quantitative, sensitive, versatile, robust. *Dev.* 2018;145(12). doi:10.1242/dev.165753.